Clim. Past, 20, 1817–1836, 2024
https://doi.org/10.5194/cp-20-1817-2024

Climate of the Past
Open Access
EGU

South Asian summer monsoon enhanced by the uplift of the Iranian Plateau in Middle Miocene

Meng Zuo[1,2], Yong Sun[3], Yan Zhao[3], Gilles Ramstein[4], Lin Ding[3], and Tianjun Zhou[1]

[1]LASG, Institute of Atmospheric Physics, Chinese Academy of Sciences, Beijing, China
[2]State Key Laboratory of Severe Weather and Institute of Tibetan Plateau Meteorology, Chinese Academy of Meteorological Sciences, Beijing, China
[3]State Key Laboratory of Tibetan Plateau Earth System, Environment and Resources (TPESER), Institute of Tibetan Plateau Research, Chinese Academy of Sciences, Beijing, China
[4]Laboratoire des Sciences du Climat et de l'Environnement, LSCE/IPSL, CEA-CNRS-UVSQ, Université Paris-Saclay, Gif-sur-Yvette, France

Correspondence: Yan Zhao (yan.zhao@itpcas.ac.cn)

Received: 5 February 2024 – Discussion started: 26 February 2024
Revised: 14 May 2024 – Accepted: 18 June 2024 – Published: 13 August 2024

Abstract. The South Asian summer monsoon (SASM) significantly intensified during the Middle Miocene (17–12 Ma), but the driver of this change remains an open question. The uplift of the Himalaya (HM) and the Iranian Plateau (IP) and global CO_2 variation are prominent factors among suggested drivers. Particularly, the impact of high CO_2 levels on the Miocene SASM has been little studied, despite the wide range of reconstructed CO_2 values around this period. Here we investigate their effects on the SASM using the fully coupled Ocean–Atmosphere Global Climate Model, CESM1.2, through a series of 12 sensitivity experiments. Our simulations show that the IP uplift plays a dominant role in the intensification of the SASM, mainly in the region around northwestern India. The effect of the HM uplift is confined to the range of the HM and its vicinity, producing orographic precipitation change. The topography forcing overall out-competes CO_2 variation in driving the intensification of the SASM. In the case of extremely strong CO_2 variation, the effects of these two factors are comparable in the core SASM region, while in the western region, the topographic forcing is still the dominant driver. We propose a thermodynamical process linking the uplift of the IP and the enhanced SASM through the release of latent heat. When compared with reconstructions, the simulated response of SASM to the IP uplift is in good agreement with observed precipitation and wind field, while the effects of the HM uplift and CO_2 variation are inadequate to interpret the proxies.

1 Introduction

The Middle Miocene (17–12 Ma) was a period characterized by major climatic, tectonic, CO_2, and environmental changes (Steinthorsdottir et al., 2021). Increasing evidence indicates that the South Asian summer monsoon (SASM) was remarkably intensified in the Middle Miocene (Clift et al., 2008; Clift and Webb, 2019; Gupta et al., 2015; Bialik et al., 2020; Vogeli et al., 2018), although its inception was no later than the Early Miocene (Ali et al., 2021; Licht et al., 2014; Farnsworth et al., 2019). However, the driving factor of its evolution remains an issue of great debate. Besides the effect of geographic change (Ramstein et al., 1997; Fluteau et al., 1999; Farnsworth et al., 2019; Thomson et al., 2021; Tardif et al., 2020, 2023; Sarr et al., 2022), the growth of the Himalaya (HM)–Tibetan Plateau (TP) (HM–TP) has traditionally been called upon for the SASM development (Clift et al., 2008; Clift and Webb, 2019; Manabe and Terpstra, 1974; Kutzbach et al., 1989; Prell and Kutzbach, 1992; Ramstein et al., 1997; An et al., 2001; Kitoh, 2002; Chakraborty et al., 2006; Wu et al., 2012; Tada et al., 2016; Tardif et al., 2020, 2023). The HM, which has long been regarded as the "southern TP" (Spicer, 2017), receives particular attention (Boos and Kuang, 2010; Wu et al., 2012; Zhang et al., 2015). Recent geological evidence (Liu et al., 2016; Ding et al., 2017, 2022) suggests that, in contrast to previous studies, the HM had risen to a height of 2.3 ± 0.9 km by the earli-

est Miocene, reaching approximately 4 km by 19 Ma. From 15 Ma onwards, the HM projected significantly above the average elevation of the plateau that had already attained its modern height before the Miocene (Wang et al., 2014). The coincidence of the ongoing HM uplift above the TP since 15 Ma and the intensification of SASM appears to support the hypothesis that the evolution of the SASM is predominantly driven by the formation of the HM–TP.

However, this traditional view is challenged by many modeling studies that emphasize the importance of peripheral mountain ranges (Chakraborty et al., 2006; Tardif et al., 2020, 2023; Sarr et al., 2022; Liu et al., 2017; Tang et al., 2013; Chen et al., 2014; Acosta and Huber, 2020). Notably, the Iranian Plateau (IP), which also underwent uplift during the same period as the Miocene SASM enhancement at around 15–12 Ma, is considered a critical factor (McQuarrie et al., 2003; Mouthereau, 2011; Ballato et al., 2017; Bialik et al., 2020), although the evolution history of the IP's buildup remains hotly debated (Agard et al., 2011; McQuarrie et al., 2003; Mouthereau, 2011; Ballato et al., 2017). Nevertheless, most studies suggest a Miocene age for the uplift of most landforms. Geological evidence indicates that in the northern sectors of the IP, the uplift likely occurred between 16.5–10.7 Ma (Ballato et al., 2017) and particularly accelerated after 12.4 Ma, while in regions bordering the IP to the south, uplift occurred between 15 and 5 Ma (Mouthereau, 2011). The Zagros orogen, a significant part of the IP, developed in three distinct pulses within the last $\sim$ 20 Ma (Mouthereau, 2011; Agard et al., 2011). Therefore, there exists significant uncertainty regarding the growth of the IP. The respective contributions of the IP and HM uplift to intensified SASM during the Middle Miocene remain unclear.

Various mechanisms were proposed to explain the linkage between the uplift of the IP and HM and the intensification of SASM rainfall. These include the mechanical blocking effect (Tang et al., 2013), topographic thermal forcing (Chen et al., 2014; Wu et al., 2012; Liu et al., 2017), and the role of a gatekeeper to insulate the pool of high-enthalpy air in northern India from westerly advection of cool and dry air (Acosta and Huber, 2020). However, most of these modeling studies have examined the effects of IP and HM uplift using the Atmospheric General Circulation Model (AOGCM) with modern geographies (Liu et al., 2017; Zhang et al., 2015; Tang et al., 2013; Acosta and Huber, 2020), potentially overlooking two key factors: (1) the neglect of air–sea interaction processes (Kitoh, 2002; Su et al., 2018) and (2) the risk of misinterpreting past changes due to the critical role of land–sea distribution in shaping the paleoclimate features (Tardif et al., 2023; Ramstein et al., 1997). Therefore, we opt to use a fully coupled Atmosphere–Ocean General Circulation Model (AOGCM) to revisit the response of the SASM to the IP and HM uplift under Miocene boundary conditions despite requiring additional computational resources.

The SASM is sensitive to changes in CO_2 concentration (Thomson et al., 2021). The effect of CO_2 variation is overall estimated to be less than that of geography and/or topography (Farnsworth et al., 2019; Thomson et al., 2021; Tardif et al., 2023); however, during the Mid- to Late Miocene, its contribution to rainfall change is comparable to that of orographic uplift – even when the CO_2 is set from 560 to 280 ppm (Thomson et al., 2021). Proxy records indicate that the Early to Middle Miocene was a warming period, which is known as the Middle Miocene Climatic Optimum ($\sim$ 17–14 Ma), followed by a Late Miocene cooling (Steinthorsdottir et al., 2021). There is large uncertainty in estimated CO_2 variation in the Middle Miocene, with a wide range of reconstructed values from $\sim$ 180 to $\sim$ 600 ppmv (parts per million by volume) (Foster and Rohling, 2013; Steinthorsdottir et al., 2021; Pagani et al., 1999; CenCO_2pip, 2023) and even to more than 1000 ppmv (Rae et al., 2021) during the Middle Miocene Climatic Optimum (MMIO). Nevertheless, according to the general concept, the atmospheric CO_2 concentration peaked around 15 Ma and then declined (CenCO_2pip, 2023). Therefore, it is necessary to re-examine the effect of CO_2 forcing on SASM rainfall based on the possible range of CO_2 variation.

In this study, we utilize a fully coupled AOGCM to explore the impact of IP and HM uplift and the CO_2 variation on the SASM. Considering that the uplift of HM and IP predominantly occurred after 15 Ma, roughly coinciding with pronounced CO_2 variations during 17–14 Ma, we conduct two sets of sensitivity experiments based on Middle Miocene geography. The topographic sensitivity experiments are placed into the context of the current understanding of the regional tectonic and geographic settings while a set of CO_2 sensitivity experiments ranging from 280 to 1000 ppmv is performed. The model configuration, Middle Miocene boundary condition, and experimental design are described in Sect. 2. In Sect. 3, we show the SASM response to IP and HM uplift and the effect of CO_2 forcing. The mechanisms responsible for the monsoonal precipitation change are examined in Sect. 4. The implication of our results to the evolution of the SASM in the Middle Miocene is discussed in Sect. 5 before giving conclusions in Sect. 6.

2 Data and methods

2.1 Climate model

The model used in this study is the Community Earth System Model (CESM), version 1.2.1, of the National Center for Atmospheric Research. It includes the Community Atmosphere Model (CAM4) (Neale et al., 2013), the Community Land Model (CLM4) (Hunke and Lipscomb, 2010), the Parallel Ocean Program (POP2; Smith et al., 2010), and the Community Ice Sheet Model and the Community Ice code (Glimmer-CICE4). Both the ice sheet model and the dynamic vegetation module (Lawrence et al., 2011) incorporated in CLM4 are switched off in this study. The horizontal resolution used is 1.9° (latitude) × 2.5° (longitude)

for CAM4 with 26 vertical levels, and CLM4 has an identical horizontal resolution. CESM has been extensively used for modern and tectonic climate studies (Chen et al., 2014; Goldner et al., 2014; Frigola et al., 2018). In general, this model simulates modern surface temperature distributions and Equator-to-pole temperature gradients well (Gent et al., 2011), although biases exist (Neale et al., 2013). However, it strongly overestimates the Miocene meridional temperature gradient compared to reconstructions, which is a thorny problem for Miocene modeling practice (Burls et al., 2021; Steinthorsdottir et al., 2021) mainly caused by the inability of climate models to reproduce polar-amplified warmth (Krapp and Jungclaus, 2011; Herold et al., 2011; Goldner et al., 2014; Burls et al., 2021). Nevertheless, the temperature biases in low latitudes are small, generally within 1 °C (Burls et al., 2021).

2.2 Boundary conditions

Our Miocene experiments are configured with geography, topography, bathymetry, and vegetation cover from Frigola et al. (2018) (henceforth F18), which provide boundary conditions for modeling studies with a focus on the Middle Miocene. According to F18, the most prominent geographic differences between the Middle Miocene and present day are the opening of the Tethys, Indonesian, and Panama seaways, the closure of the Bering Strait, and lower elevations of most of the highest regions of the globe. For instance, the African topographies were reduced to 25 % of their current elevation (Fig. 1a and b).

The topography of the Tibetan Plateau in F18 is set to its estimated Early to Middle Miocene elevation. The southern and central plateau reached a near-modern elevation; the northern plateau is set to 3–4 km, but its northward extend is reduced to reflect the rapid uplift occurring in the Pliocene (Harris, 2006). The HM reached to 60 %–80 % of its present height. As for the IP, here we lumped together all the mountain ranges west of the Himalaya, including the Hindu Kush region and Pamir as the IP. In F18, the northern part of the IP reached a near-modern elevation at 1000–2000 m, but its southern part was lower than 1000 m.

The Miocene vegetation is prescribed as that in F18, which is a global gridded distribution (Fig. S1 in the Supplement) merging previous reconstructions (see F18 for more details). During the Miocene, vegetation types associated with lower latitudes today encroached on higher latitudes. There was reduced presence of ice compared to modern conditions, and ice-free regions were covered by tundra in Antarctica while cold, mixed forests spread over Greenland.

2.3 Experimental design

We first perform two simulations: the pre-industrial (piControl) and the Middle Miocene (MMIO) simulation, which differ in their applied geography (Fig. 1a and b), bathymetry, vegetation cover, and the CO_2 concentrations, while the solar constant, orbital configuration, and the concentrations of other greenhouse gases are kept at their modern values. The CO_2 concentration is set to 280 ppmv in the piControl (Eyring et al., 2016) and 400 ppmv in the MMIO, following the setting of F18. The choice of 400 ppmv is somewhat low but within the range of published estimates (see details in F18 and Burls et al., 2021). Both simulations are integrated to reach quasi-equilibrium, and particularly the MMIO experiment is integrated ca. 3000 years. The difference between MMIO and piControl provides the background information of the simulated changes in the SASM between the two periods.

Starting from the MMIO simulation, we run a set of experiments with altered orography in the HM and the IP. We examine the joint effects of the HM and IP on the SASM, assuming the HM and the IP rise simultaneously from flat (0 %) to 100 % of their reference height (Fig. 1c and d). The reference height is the modern altitude for the HM and the reconstructed Miocene altitude for the IP. The experiments are referred as IP0HM0 and IP100HM100, respectively. To further separate the climatic effect of the IP and HM uplift, we conduct another two experiments, namely IP100HM0 and IP0HM100. In the former (latter) experiment, the HM (IP) is absent, while the IP (HM) reaches its reference height (Fig. 1e and f). Combined with the experiments of IP0HM0 and IP100HM100, the effect of elevated IP and HM is estimated (see Sect. 3.2). To further reveal the impact of the IP uplift on the SASM evolution, two other experiments are conducted, namely IP50HM0 and IP50HM100, indicating that the IP is reduced by half of its Miocene height while the HM is absent and fully uplifted, respectively.

To clarify the relative role of CO_2 forcing on SASM rainfall in the Middle Miocene, we also run a set of CO_2 sensitivity experiments with the CO_2 setting at 280, 560, 800, and 1000 ppmv, referred to as MMIO280, MMIO560, MMIO800, and MMIO1000, respectively. The high values of 800 and 1000 ppm are chosen because new reconstructions of CO_2 generally corresponded to 3 times the pre-industrial levels (Rae et al., 2021). These experiments have the same boundary conditions as the MMIO simulation, differing only in CO_2 concentration.

The simulations considered in our study are listed in Table 1. The sensitivity experiments are integrated from the MMIO equilibrium state for another 200 (500) years for the topography (CO_2) sensitivity experiments to reach quasi-equilibrium. The final 50 years of these simulations are used for analysis.

2.4 South Asian summer monsoon indices

The following indices are defined to illustrate features of the SASM changes.

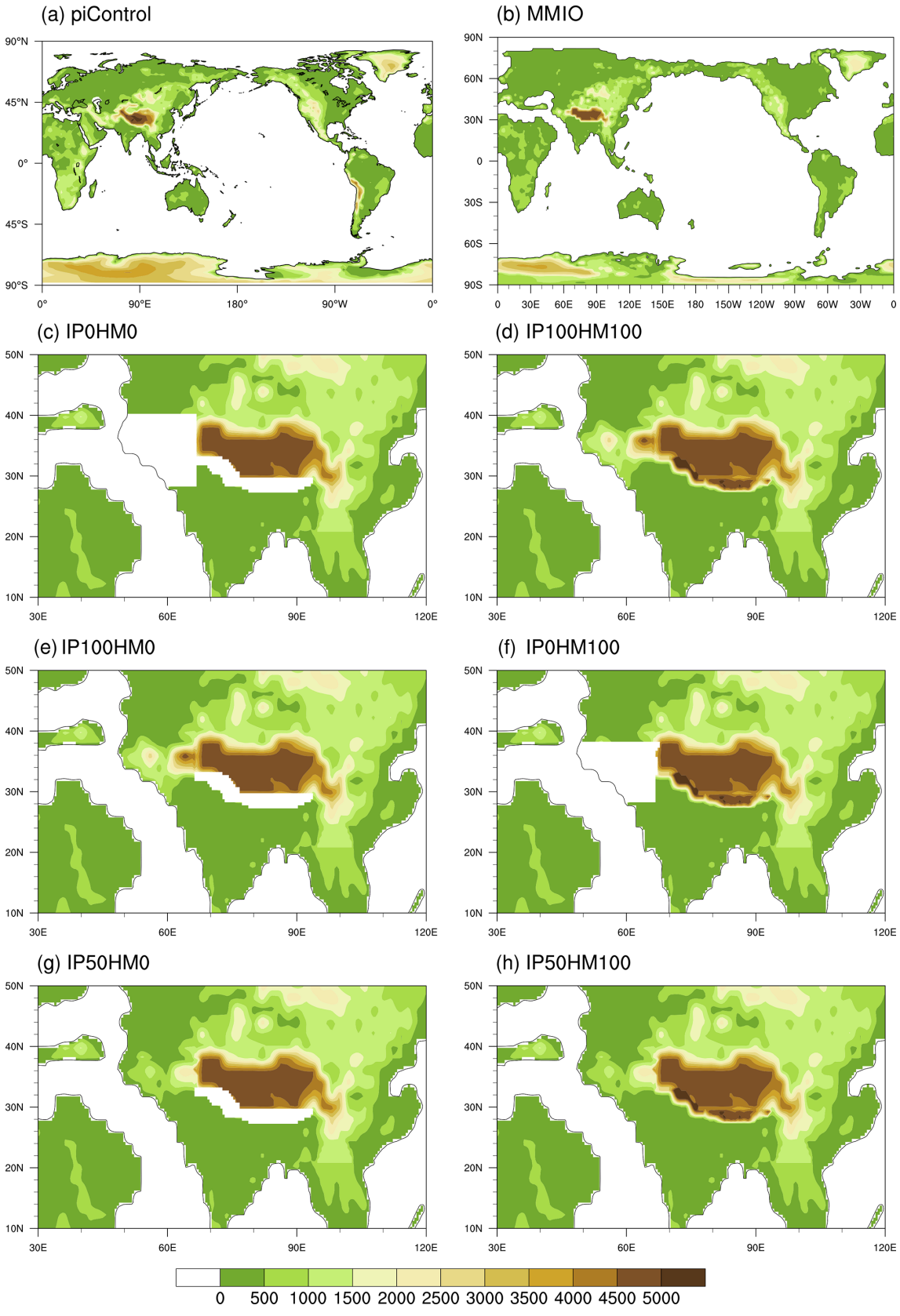

Figure 1. Topography of **(a)** piControl, **(b)** MMIO, and orographic sensitivity experiments, including **(c)** IP0HM0, **(d)** IP100HM100, **(e)** IP100HM0, **(f)** IP0HM100, **(g)** IP50HM0, and **(h)** IP50HM100. (The maps are plotted at $0.5° \times 0.5°$ resolution. The same maps but at $1.9° \times 2.5°$ resolution are provided in Fig. S2.)

Table 1. Simulations performed with CESM1.2 in this study. See Fig. 2 for modern and paleogeographical maps.

Experiment	Geography	Vegetation	CO_2 (ppm)	IP	HM
piControl	Modern	Modern	280	Modern	Modern
MMIO (IP100HM80)	M. Miocene[a]	M. Miocene	400	M. Miocene	M. Miocene
IP0HM0	M. Miocene	M. Miocene	400	0	0
IP50HM0	M. Miocene	M. Miocene	400	50 %	0
IP100HM0	M. Miocene	M. Miocene	400	100 %	0
IP0HM100	M. Miocene	M. Miocene	400	0	100 %[b]
IP50HM100	M. Miocene	M. Miocene	400	50 %	100 %
IP100HM100	M. Miocene	M. Miocene	400	100 %	100 %
MMIO280	M. Miocene	M. Miocene	280	M. Miocene	M. Miocene
MMIO560	M. Miocene	M. Miocene	560	M. Miocene	M. Miocene
MMIO800	M. Miocene	M. Miocene	800	M. Miocene	M. Miocene
MMIO1000	M. Miocene	M. Miocene	1000	M. Miocene	M. Miocene

[a] M. Miocene is for Middle Miocene. [b] 100 % of the height of modern HM.

1. *All-Indian rainfall (AIR)*. This is the regional summer mean precipitation over the land points within the domain of 7–30° N, 65–95° E. It represents the precipitation in the core region of the SASM.

2. *Webster–Yang index (WYI; Webster and Yang, 1992)*. This is the meridional wind stress shear between 850 and 200 hPa (averaged over 0–20° N, 40–110° E) during June–August.

3. *Somali jet strength (SMJ; Sarr et al., 2022)*. This is the maximum intensity of the Somali jet over the Arabian Sea (averaged over 0–20° N, 30–60° E) during June–August.

2.5 Moisture budget analysis

Moisture budget analysis (MBA) can decompose the precipitation change into changes in evaporation and moisture advection (Chou et al., 2009). It relates the net precipitation (precipitation minus evaporation; $P - E$) to the vertically integrated moisture flux convergence. More details about MBA are given in Sect. S2. This method has been widely applied to paleoclimate studies in recent years, such as distinguishing the physical processes involved in precipitation changes in the Mid-Holocene (Sun et al., 2023). Here, we apply a MBA to reveal the physical processes related to SASM precipitation responses to the uplift of IP–HM and to CO_2 change.

3 Results

3.1 Climatology of the SASM in the present day and Middle Miocene

The CESM1.2 is one of the best models for simulating the present-day SASM (Anand et al., 2018; Jin et al., 2020). The CESM1.2 reproduced the broad features of the SASM system, including the onshore flows and strong monsoonal precipitation, when compared to the observational datasets, including the Global Precipitation Climatology Project (GPCP) (precipitation) and ERA5 (circulation) (Huffman et al., 2009; Hersbach et al., 2020). The maximum centers of precipitation are reasonably captured over the southern slope of the HM, the east Arabian Sea, and the Bay of Bengal despite biases in intensity and extensions (Fig. 2a and b), which is largely due to the coarse spatial resolution (Acosta and Huber, 2017; Anand et al., 2018; Botsyun et al., 2022a, b; Boos and Hurley, 2013). Thus, we focus on the large-scale circulations and treat the local features with caution. The regional summer mean precipitation, as measured by the AIR, is 7.7 mm d^{-1} in GPCP and 8.7 mm d^{-1} in the piControl experiment. The positive bias reflects an overestimation of precipitation in the Western Ghats and at the HM foothills.

Compared with the piControl experiment, the MMIO simulation displays apparent adjustment of the JJA mean low-level circulation. The westerlies pass Africa into the Indian region, and a cyclonic circulation develops over the Arabian Sea; then, the cross-equatorial flow weakens and displaces southward (Fig. 2c). There is a considerable enhancement of monsoonal precipitation in South Asia, but it is not limited there (Fig. 2c). AIR in the MMIO simulation is 10.4 mm d^{-1}, which is $\sim$ 20 % higher than that in the piControl experiment.

The wetter Miocene climate is also reflected by the widespread Afro–Asian monsoon, which was suggested by previous modeling studies (Herold et al., 2011; Zhang et al., 2015). Here a monsoon-like climate is defined as the local (summer minus winter) precipitation exceeding 2 mm d^{-1} and as the local summer precipitation exceeding 55 % of the annual total (Wang and Ding, 2008). This monsoon index is determined by the intensity of the summer monsoonal precipitation in the region of the South Asian Monsoon (SAM). Compared with the present day, the domain of the SAM ex-

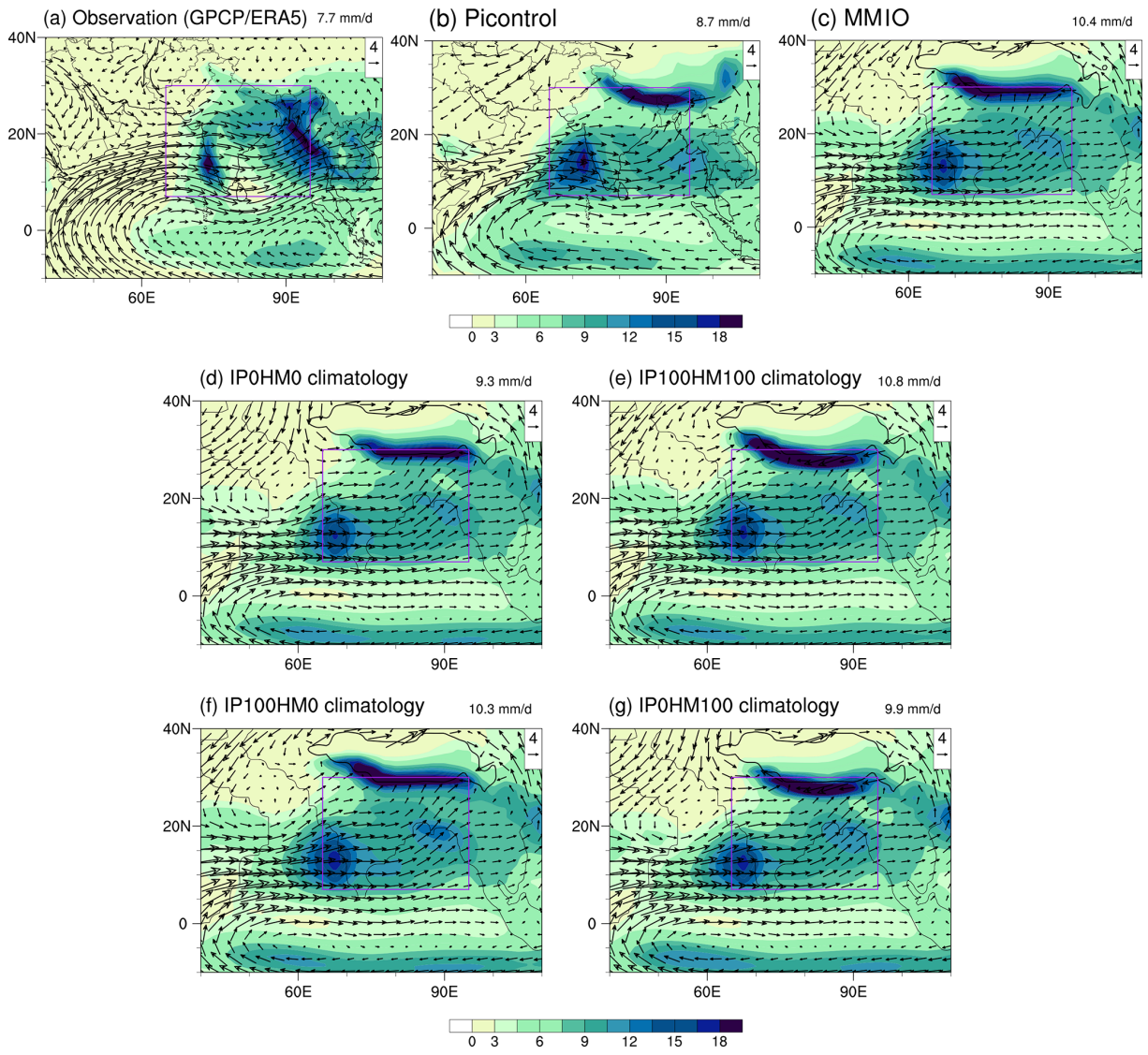

Figure 2. Climatology of JJA (June–July–August) seasonal mean South Asia summer monsoon (SASM) precipitation (mm d^{-1}) and 850 hPa winds (vectors; m s^{-1}) from the **(a)** observation precipitation from GPCP and circulation from ERA5. **(b)** Preindustrial control experiment and **(c)** MMIO experiment. **(d)** IP0HM0, **(e)** IP100HM100, **(f)** IP100HM0, and **(g)** IP0HM100. Climatology is the average over 1979–2005 for the observation. As for the piControl and MMIO experiments, we select the last 50 and 100 years of simulation, respectively. All-Indian rainfall (AIR) is shown at the top right of each panel. AIR indicates precipitation over the land points within the purple square in each panel (7–30° N, 65–95° E). The black contour in panels **(c)**–**(g)** indicates the altitude of 2500 m.

tends westward both on land and over the Arabian Sea, where it nearly connects the African monsoon (Fig. 3c). Interestingly, this characteristic is also noted in the Miocene study of Fluteau et al. (1999), despite significant differences in the climate model and paleogeography employed in the two studies. The distribution of the simulated SAM is generally consistent with the proxies (Table 2), confirming the wide existence of SAM in the Middle Miocene in terms of rainfall seasonality.

3.2 The effect of the HM and IP uplift

We first examine the effect of the joint uplift of the HM and IP (hereafter referred to as IP–HM). With the uplift of the IP–HM (Fig. 4a), a prominent cyclonic anomaly is built to the west of the IP with the intensified southwesterlies from Africa via the Arabian Sea into the northwestern India. Increased precipitation is found along the eastern flank of the cyclonic anomaly to the slopes of the western HM and northeastern IP. In the eastern part of the monsoon region, the enhanced precipitation occurs mainly along the southern edge

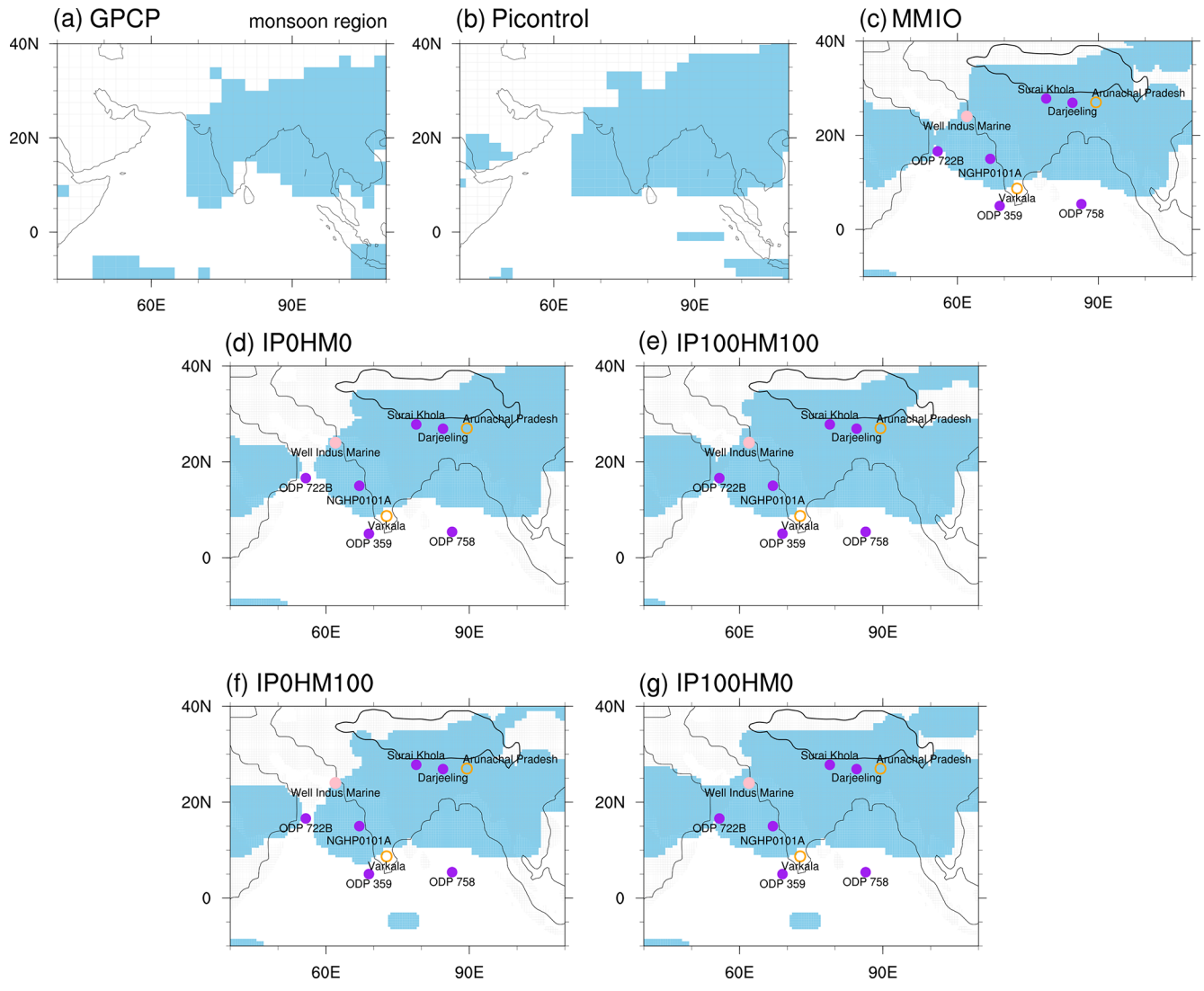

Figure 3. The monsoon domains (blue shading) in the **(a)** GPCP, **(b)** piControl, **(c)** MMIO, **(d)** IP0HM0, **(e)** IP100HM100, **(f)** IP0HM100, and **(g)** IP100HM0 experiments, which are defined by the regions where local (summer minus winter) precipitation exceeds 2 mm d^{-1} and the local summer precipitation exceeds 55 % of the annual total. Dots in panels **(c)**–**(g)** represent reconstructions near the SASM region, solid purple dots denote enhanced SASM, orange circles denote no significant change, and solid pink dots denote weakened SASM from the Middle to Late Miocene. The black contour in panels **(c)**–**(g)** indicates the altitude of 2500 m.

of the HM while the leeward side features a remarkably decreased precipitation, indicating the rain shadow effect.

Corresponding to the summer precipitation change in response to IP–HM uplift, the domain of the SASM expands westward over the Arabian Sea and the Indian subcontinent (Fig. 3d and e). The western extension over land is about 65° E in the IP0HM0 experiment and reaches 60° E in the IP100HM100 experiment, indicating that the change in the SASM is significant in the northwest of the Indian subcontinent. Interestingly, monsoonal signal exists in the IP0HM0 experiment, an analogue to the "Early Miocene", indicating that the proto-monsoon exists by having TP only, which is also found in previous studies (Sarr et al., 2022). At the site of ODP 722B, the monsoonal signal is absent in IP0HM0 (Fig. 3d) but present in IP100HM80 (MMIO; Fig. 3c) and IP100HM0 (Fig. 3e) when the IP–HM is uplifted.

We further separate the effect of the IP and HM uplift. The climate response to IP uplift (IP100-IP0) is estimated as $((\text{IP100HM0}-\text{IP0HM0})+(\text{IP100HM100}-\text{IP0HM100}))/2$. Similarly, the effect of HM uplift HM100-HM0 is estimated as $((\text{IP0HM100}-\text{IP0HM0})+(\text{IP100HM100}-\text{IP100HM0}))/2$. The changes in precipitation and low-level circulation much resemble that attributing to the IP–HM uplift (Fig. 4a), indicating that by itself, the IP can sustain major parts of the precipitation changes except over the central–eastern HM. The easterly anomaly across the Indian subcon-

Table 2. Evidence of modern SAM in Middle Miocene from recently published studies. ODP represents the Ocean Discovery Program.

No.	Station	Location (lat/long)	Proxies	Intensification age (Ma)	Trend*	Variable	References
1	Well Indus Marine A-1	24/66	Weathering	15–12	Decreasing	Precip.	Clift et al. (2008)
2	ODP 359	5/73	Sedimentary and geochemical record	12.9	Increasing	Wind	Betzler et al. (2016)
3	ODP 722B	16.6/59.8	Bio-marker	12.9	Increasing	Wind	Gupta et al. (2015)
	ODP 722B	16.6/59.8	Bio-marker	14	Increasing	Wind	Bialik et al. (2020)
4	NGHP-01-01A	15/71	Bio-marker	14	Increasing	Precip.	Yang et al. (2020)
5	Varkala	8.7/76.7	Pollen fossil	17–15	No change	Precip.	Reuter et al. (2013)
6	ODP 758	5.4/90.4	Weathering	13.9	Increasing	Wind	Ali et al. (2021)
7	Surai Khola	27.8/83	Leaf fossil	13	Increasing	Precip.	Srivastava et al. (2018), Bhatia et al. (2021)
8	Darjeeling	27/88.5	Leaf fossil	13	Increasing	Precip.	Toohey et al. (2014)
9	Arunachal Pradesh	27/93.5	Leaf fossil	13	No change	Precip.	Toohey et al. (2014)
	Arunachal Pradesh	26/93.5	Weathering	13	No change	Precip.	Vogeli et al. (2018)

* Trend of monsoon index change from Middle to Late Miocene.

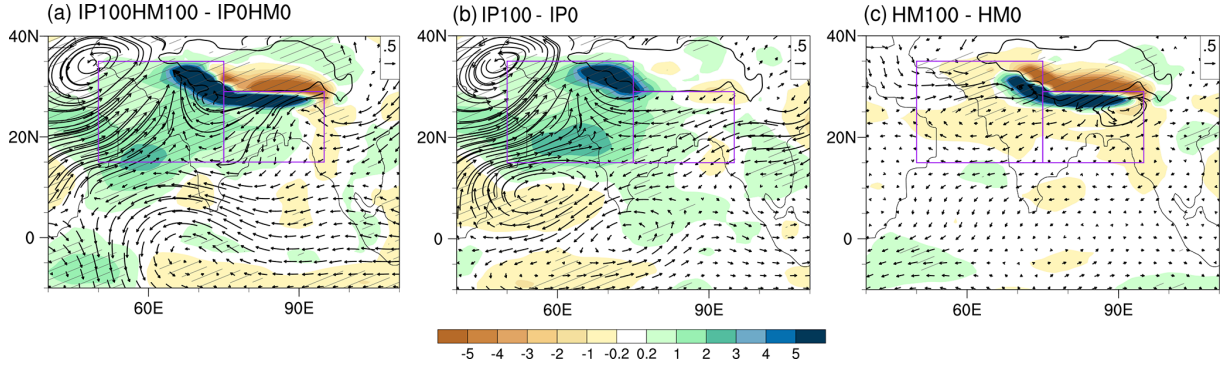

Figure 4. Precipitation (shaded; mm d^{-1}) and 850 hPa wind differences between the **(a)** IP100HM100 and IP0HM0 experiments, **(b)** IP100 and IP0 experiments, and **(c)** HM100 and HM0 experiments. Here IP100 − IP0 = ((IP100HM0 − IP0HM0) + (IP100HM100 − IP0HM100))/2, HM100 − HM0 = ((IP0HM100 − IP0HM0) + (IP100HM100 − IP100HM0))/2. The black contour in each panel indicates the altitude of 2500 m. Purple boxes represent western (15–35° N, 50–75° E) and eastern (15–29° N, 75–95° E) parts of the South Asian monsoon region. Slashes indicate values at the > 95 % confidence level based on Student's *t* test.

tinent indicates that the westerly is blocked by the elevated IP from northern India, facilitating moisture convergence and rainfall increase over the northern Indian continent. As a result, the regional mean precipitation increases by 1.1 and 2.0 mm d^{-1} over the core (7–30° N, 65–95° E) and western regions (15–35° N, 50–75° E), respectively.

In contrast to the widespread effect of the IP on the SASM, the HM uplift only has a local effect (Fig. 4c), which is mostly confined to the HM and its close vicinity, and the change in low-level circulation is noisy and weak. The precipitation strongly increases along the southern slope of the HM and dramatically decreases on its leeward side, resembling the changes in precipitation in the eastern region caused by the IP–HM uplift. As a result, there is little change in the regional mean precipitation over the core and eastern regions (15–35° N, 75–95° E). Specially, the changes in precipitation patterns and low-level circulation between IP100HM100 and MMIO (not shown) closely resemble that shown in Fig. 4c, albeit with reduced intensity, indicating that further uplift of HM above the TP does not result in an intensified SASM.

In summary, the joint influences of the IP–HM uplift on the SASM are the superimposed effect of the IP and HM. In the western region, i.e., from the Arabian Sea to northwestern India and Pakistan, the IP plays a dominant role, while in the eastern region, i.e., the eastern part of South Asia, the changes in the SASM mainly attribute to the HM uplift. And the western extension of the SASM domain over the Arabian Sea and the Indian subcontinent is mainly caused by the uplift of IP rather than HM (Fig. 3f and g).

3.3 The effects of the CO_2 forcing vs. topographic forcing

To illustrate the effect of CO_2 forcing on SASM during the MMIO, we show the climatology of the SASM at low and high levels of CO_2 concentration based on MMIO280 and MMIO1000 experiments, respectively (Fig. 5). The spatial circulation patterns in these two experiments are similar to that in the MMIO, but the magnitudes change significantly (Figs. 5a, b and 2c). With the increase in CO_2, the meridional cross-equatorial flow slightly strengthens along the east African coast until 15° N but weakens to the east (Fig. 5c and d), leading to little change in the regional mean strength of this flow over the Arabian Sea. Meanwhile, precipitation enhances along the band of 15–25° N but decreases to the south, indicating a northward shift in the tropical rainfall belt. As the CO_2 rises from 280 to 400 ppm, and subsequently to 1000 ppm, the AIR index correspondingly increases by 0.5 and 1.2 mm d^{-1}, respectively. MBA (Sect. S2) further reveals that the increased monsoonal precipitation is primarily induced by enhanced thermodynamic conditions due to atmospheric warming, while the contribution from the change in large-scale monsoon circulation plays a secondary role (Fig. S5c and d). For instance, the precipitation change between MMIO1000 and MMIO in the core SASM region is 1.2 mm d^{-1}, of which 0.6 is from the thermodynamical processes related to changes in moisture, and 0.25 mm d^{-1} is from the dynamical processes related to circulation change.

To compare the effect of CO_2 forcing versus topographic forcing on the SASM, we examine the changes in precipitation and low-level circulation between MMIO1000 and IP0HM0 experiments (Fig. 5e), which actually reflects the combined effects of the CO_2 forcing (MMIO1000–MMIO) and IP–HM uplift (MMIO–IP0HM0). It is clear that the SASM changes in Fig. 5e bear the features of Figs. 5d and 4a, with precipitation enhancing along the band of 15–25° N and reducing to the south in response to increased CO_2 and a prominent cyclonic anomaly built to the west of the IP in response to the IP–HM uplift. Moisture budget analysis further reveals that the enhanced precipitation of 3.2 mm d^{-1} in the western part of the SAM region is equally attributed to the vertical and horizontal moisture advection of 2.3 mm d^{-1} (Fig. 6). The moisture advection by anomalous meridional winds is the dominant contribution term, which is actually the response to the IP uplift as seen in Sect. 4.

We further examine the impacts of CO_2 forcing and topographic forcing in terms of WYI, SMJ, AIR (Sect. 2.4), and the mean precipitation over the western part of the SASM region (Fig. 7). Under the topographic forcing, WYI exhibits small changes, with the exception of a relatively lower value in the IP0HM100 experiment. Concurrently, both precipitation and low-level circulation indices increase in response to the IP uplift, indicating a quasi-circulation–rainfall coupling relationship. With the increasing CO_2 forcing, there is a noticeable decrease in WYI, whereas AIR and the precipitation in the western SAM region increase significantly, indicating a decoupling relationship between large-scale circulation and monsoonal rainfall. The cross-equatorial flow at the lower level (Somali jet) is insensitive to CO_2 change, as already shown in Fig. 5.

The maximum difference in each index across the set of CO_2 or topographic sensitivity experiments is defined as the effect of each driver. In terms of WYI (Fig. 7a), the effect of CO_2 forcing is $\sim$ 150 % greater than that of IP–HM forcing, with values of 2.5 m s^{-1} vs. 1.0 m s^{-1}. According to the AIR, the influence of CO_2 forcing is $\sim$ 1.5 mm d^{-1}, which is comparable to that of IP–HM forcing ($\sim$ 1.5 mm d^{-1}) but is larger than the individual contributions of IP forcing ($\sim$ 1.0 mm d^{-1}) and HM forcing ($\sim$ 0.5 mm d^{-1}). In the western region, the effect of CO_2 forcing is about 75% compared to that of IP forcing ($\sim$ 1.5 mm d^{-1} vs. $\sim$ 2.0 mm d^{-1}). In summary, CO_2 forcing is the dominant driver for large-scale monsoon circulation, while the uplift of the IP exerts a more significant effect on regional circulation and the associated precipitation.

We note that the SASM response to CO_2 forcing in the Middle Miocene is very similar to its response to future climate change. For instance, increased SASM precipitation occurring with decreased WYI is also projected under the abrupt quadrupling of CO_2 (Kong et al., 2022). The low-level

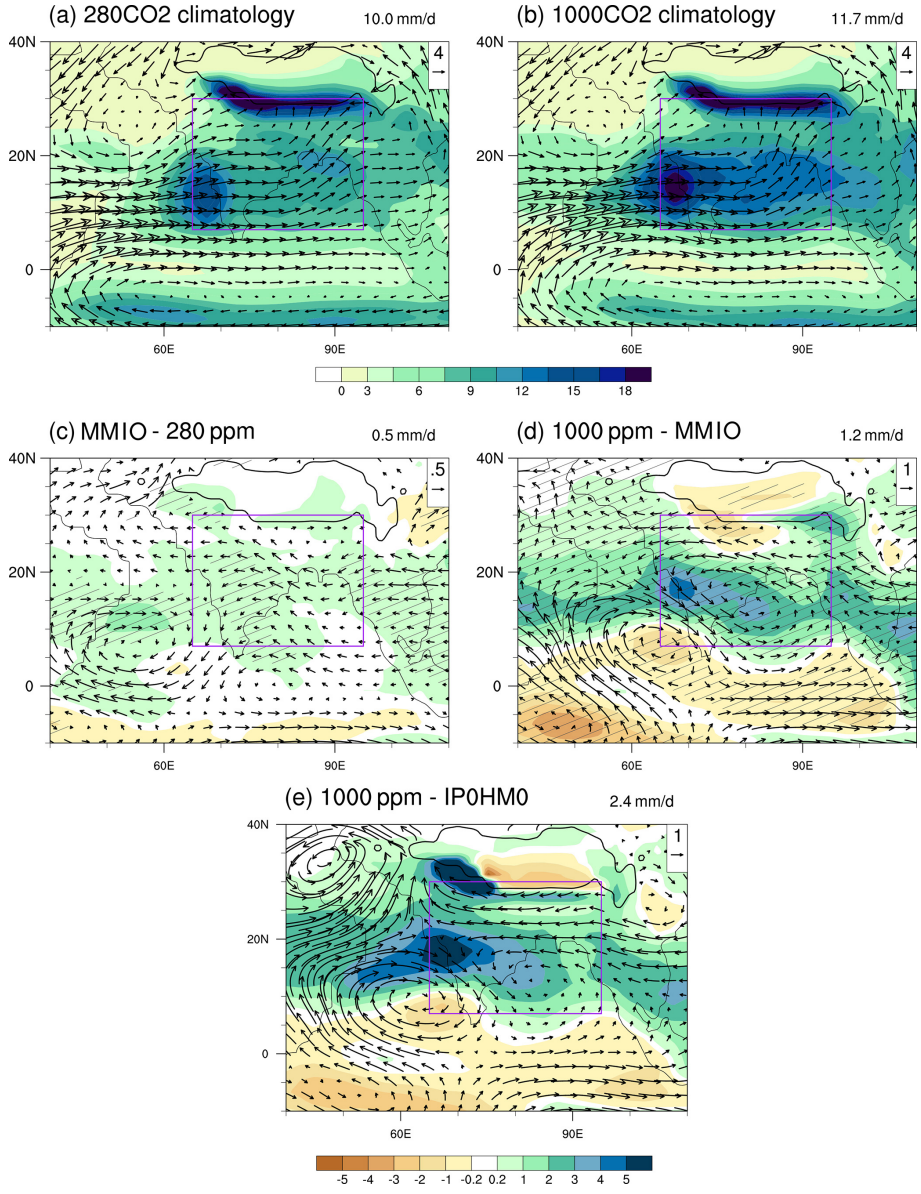

Figure 5. Climatology of JJA (June–July–August) mean South Asia summer monsoon (SASM) precipitation (mm d^{-1}) and 850 hPa winds (vectors; m s^{-1}) from the **(a)** MMIO_280 and **(b)** MMIO_1000 experiments. Precipitation (shaded; mm d^{-1}) and 850 hPa wind differences (vector; m s^{-1}) between **(c)** MMIO and MMIO_280 experiments, **(d)** MMIO_1000 and MMIO experiments, and **(e)** MMIO_1000 and IP0HM0 experiments.

monsoon circulations are projected to slightly weaken, consistent with the little change in the intensity of the low-level cross-equatorial flow in our Miocene simulations (Figs. 5 and 6). Based on an analysis across 20 climate models, Endo and Kitoh (2014) concluded that in a warmer world, the projected increase in SASM precipitation is mainly attributed to thermodynamic processes. This finding aligns with our MBA result (Fig. S5 in the Supplement). The similarity of the SASM response to changes in CO_2 implies the presence of a comparable physical mechanism operating during the two warm periods.

4 Mechanisms of the IP uplift on the SASM precipitation

To understand the mechanism of increased precipitation caused by IP uplift and HM uplift, we first use the moisture budget decomposition to identify the major moisture contributors. Here we provide the main analysis results (Fig. 8), and more details are seen in Sect. S2. To focus our analyses on atmospheric dynamics, we neglect the contribution of evaporation, which is relatively small in our simulation, despite the possibly important role of precipitation in north-

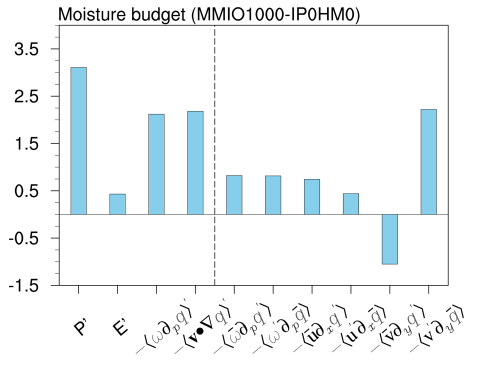

Figure 6. Moisture budget for regional mean precipitation differences (mm d^{-1}) over the western part (15–35° N, 50–75° E) of the South Asian monsoon region between MMIO1000 and IP0HM0 experiments.

western India (Zhang et al., 2019). In response to IP uplift, the increased precipitation (2.0 mm d^{-1}) is largely attributed to the horizonal moisture advection (2.1 mm d^{-1}), in particular the moisture advection by anomalous meridional winds, while the vertical advection plays a secondary role (1.1 mm d^{-1}). In response to HM uplift, the precipitation change (ca. 1.2 mm d^{-1}) is mainly caused by the vertical moisture advection (0.9 mm d^{-1}) and is offset by the horizontal moisture advection (−0.4 mm d^{-1}). Its dominant contributor is a nonlinear term involving strong interactions between the vertical motion anomalies and moisture change (see Sect. S2).

We then examine the responses of the monsoon-relevant variables to the uplifts of the IP and HM and the involved physical processes with a focus on the effect of the IP. With IP uplift, the air of the high equivalent potential temperature (θ_e) at the lower troposphere is accumulated in the IP and the surrounding region (Fig. 9a). The increased θ_e attributes to the enhancement of specific humidity (Fig. 9b), as moisture is advected by the anomalous southwesterly from North Africa via the Arabian Sea into northwestern India and Pakistan (Fig. 9b); meanwhile, it increases the convective instability. When triggered by surface sensible heating (Wu et al., 2012; Medina et al., 2010), convection takes place. At 500 hPa, the upward motion anomalies are found over the IP and along the HM (Fig. 9c), reflecting the lifting effect of the elevated topography. The height of the lifted condensation level (LCL) is significantly reduced over the IP and along the western edge of the HM (Fig. 9d), which likely resulted from the elevated surface sensible heating (He, 2017). Reduced LCL facilitates the occurrence of moist convection, further warming the air parcels by the released latent heating. Consequently, specific humidity and θ_e further increase in the middle troposphere (Fig. 9e), which in turn favors the convection activity. The pattern match between the specific humidity and θ_e indicates that the increased θ_e is primarily contributed by the increase in specific humidity and then by the warming (Fig. 9c). At the upper troposphere, forced by the latent heating, the warm-centered South Asian high strengthens over the IP (Fig. 9f), which is coupled with the cyclonic anomaly at a low level (Fig. 9b), leading to moisture convergence over the western region and accelerating the convection activity. Positive feedback is thus built between the precipitation and circulation. Regarding HM uplift, there is not a circulation adjustment between the low and high levels; the precipitation–circulation coupling thus cannot be built.

In this thermodynamical process, the IP's blocking/mechanical effect is also noticeable as it blocks the cold, dry, and extratropical air from northern India where the air of high θ_e cumulates (Fig. 9a). However, this effect is relatively weak given the small contribution of the easterly anomaly to precipitation increase (less than 0.3 mm d^{-1}; see Fig. 8a; $-\langle u'\partial_x\overline{q}\rangle$) according to the moisture budget.

5 Discussion

5.1 Application to monsoonal reconstructions

A remarkable intensification of the SASM in the Middle Miocene is revealed by increasing evidence (Fig. 3c; Table 2). In western India and the Arabian Sea, monsoon-like precipitation appeared in the Early Miocene (Clift et al., 2008; Reuter et al., 2013; Ali et al., 2021) and intensified at ∼ 15–12 Ma (Clift et al., 2008; Yang et al., 2020). In eastern India, the intensification of SASM occurred at ca. 15 Ma (Toohey et al., 2014) to ∼ 13–11 Ma (Bhatia et al., 2021; Vogeli et al., 2018). In terms of the wind system, a weaker "proto-monsoon" existed between 25 and 12.9 Ma (Betzler et al., 2016), and an abrupt intensification occurred at 12.9 Ma, as inferred from the sedimentary records in the Maldives and in the western Arabian Sea (Gupta et al., 2015), indicating the inception of a modern Somali jet. Besides, monsoonal upwelling and thus possibly the strengthening of wind speed in the western Arabian Sea has been observed since ca. 14.8 Ma.

Our modeling results support the existence of the SASM (Clift et al., 2008) in terms of precipitation seasonality in the Early Miocene; this is represented by the IP0HM0 experiment when the proto-TP existed while the IP and HM were low (Fig. 3). With the uplift of the IP rather than the HM during Middle Miocene, monsoonal precipitation increased in the northwest of the Indian landmass, as shown in the ∼ IP50, ∼ HM50 and IP100HM100 experiments (Fig. 6), corroborating the hypothesis that increased sedimentary and weathering fluxes between 25 and 15 Ma could be partially linked with monsoon intensification related to the coeval of IP–HM (Clift et al., 2008). Meanwhile, with the deepening of the cyclonical anomaly over the west of the IP (Fig. 4b), the southwesterly wind strengthens over the western Arabian Sea, which somewhat agrees with the reconstructions that suggest the inception of a modern Somali jet (Betzler et al., 2016). But the inception of the modern Somali jet is more likely attributed

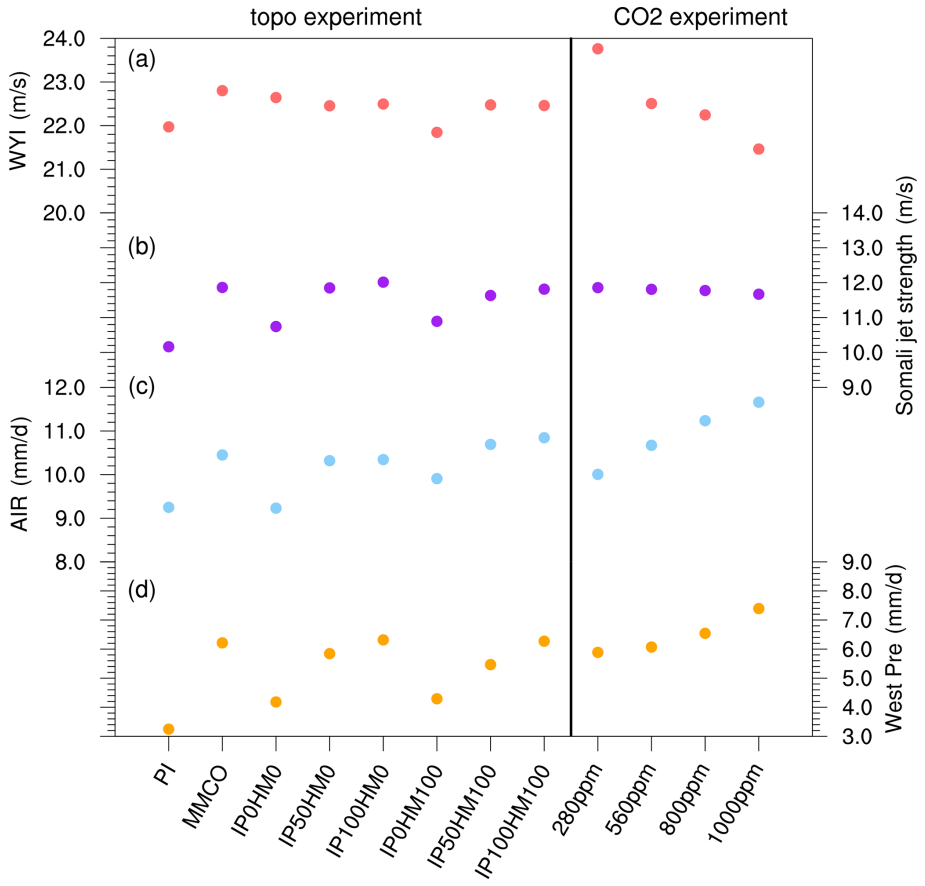

Figure 7. South Asian summer monsoon circulation and precipitation response in sensitivity experiments. Left: topography experiments. Right: CO_2 experiments. **(a)** Webster–Yang Index (meridional wind stress shear between 850 and 200 hPa, averaged over 0–20° N, 40–110° E, during June–August). **(b)** Maximum intensity of the Somali jet over the Arabian Sea (averaged over 0–20° N, 30–60° E, during June–August). **(c)** Regional mean precipitation over the land points within the domain (7–30° N, 65–95° E) named the all-Indian rainfall (AIR). **(d)** Precipitation over the western part of South Asian summer monsoon region.

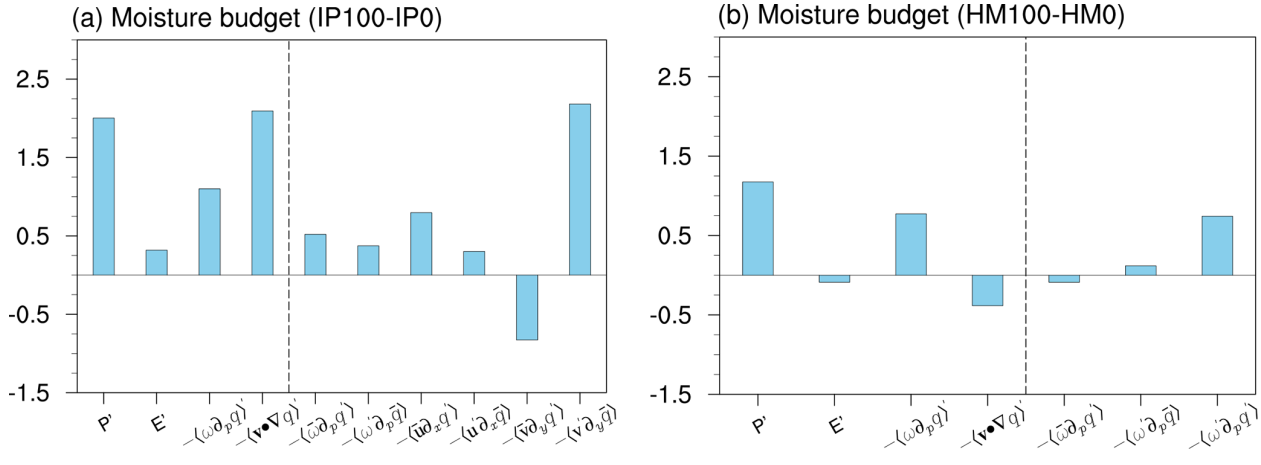

Figure 8. Moisture budget for regional mean precipitation differences (mm d^{-1}) over **(a)** the western part (15–35° N, 50–75° E) of the South Asian monsoon region between the IP100 and IP0 experiments and **(b)** the eastern part (15–29° N, 75–95° E) of the South Asian monsoon region between HM100 and HM0 experiments.

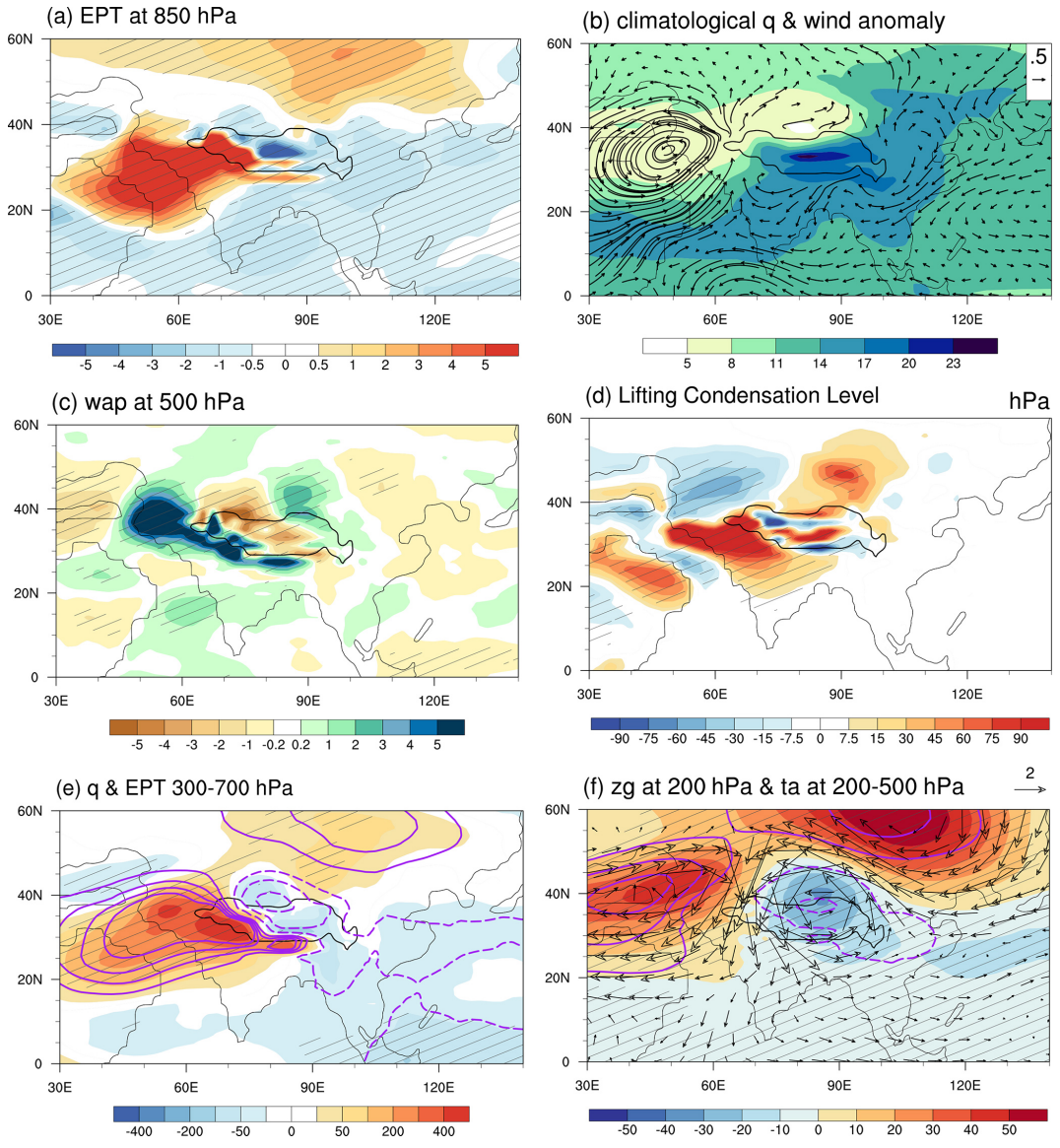

Figure 9. The differences in the JJA mean thermal dynamical and dynamical variables between IP100HM100 and IP0HM0 simulations. **(a)** Equivalent potential temperature (EPT; shading; unit: K) at 850 hPa. **(b)** Climatological specific humidity q (shading; g kg^{-1}) and wind differences (vector; unit: m s^{-1}) at 850 hPa. **(c)** Vertical velocity in the pressure coordinate (-10^{-2} Pa s^{-1}) at 500 hPa. **(d)** Lifting condensation level (LCL; unit: hPa; positive value represents lower LCL). **(e)** Specific humidity (shading) and EPT (contours; unit: K) integrated between 300 and 700 hPa. **(f)** Geopotential height z_g (shading; unit: m), temperature anomalies (contours; unit: K), and wind (vector; unit: m s^{-1}) at 200 hPa.

to the uplift of the east African topography demonstrated in modeling studies (Chakraborty et al., 2006; Sarr et al., 2022; Tardif et al., 2023; Wei and Bordoni, 2016) and/or the emergence of land in the east Arabian Peninsula (Sarr et al., 2022). This aligns with geological evidence indicating that eastern Africa began to uplift in the Late Oligocene–Early Miocene and rapidly uplifted in the Middle–Late Miocene (Macgregor, 2015). We conduct a series of complementary experiments (Sect. S3) and confirm that the elevated east African highlands play an essential role in producing the modern-like Somali jet. Meanwhile, it creates an anti-cyclonic anomaly over the north Arabian Sea, as revealed by previous studies, leading to reduced moisture transport into Indian landmass and thus decreased monsoonal precipitation. Therefore, there is likely a complementary and competing effect on the SASM evolution between the uplift of the IP and the east African highlands.

The enhanced precipitation at 13 Ma is inferred from leaf fossil in the eastern HM, which has been attributed to the rise in the HM (Toohey et al., 2014; Bhatia et al., 2021).

But this hypothesis cannot be supported by our sensitivity experiment nor can it be interpreted by the uplift of the IP based on our simulations. In contrast, some modeling studies suggested enhanced precipitation along the HM in response to mountain uplift in the American region and the northern TP (Chakraborty et al., 2006; Miao et al., 2022). Therefore, remote impacts on precipitation change in the eastern HM should be taken into account.

The CO_2 forcing has little impact on the intensity of the Somali jet, indicating its small contribution to the strengthening of surface wind inferred from the reconstructions (Gupta et al., 2015), but its effect on precipitation is likely to superimpose on that of the IP uplift. It is speculated that during the early part of the Middle Miocene Climatic Optimum, an abrupt rise in the CO_2 amplifies the effect of the IP uplift, leading to the markedly intensified SASM precipitation at around 15 Ma, as depicted in reconstructions (Clift et al., 2008; Yang et al., 2020). During the Mid–Late Miocene, the decreasing tendency of CO_2 offsets the effect of the IP uplift, although precipitation still intensifies due to the dominant impact of the latter. Given the wide range of reconstructed CO_2 in terms of intensity and timing during the Middle Miocene, the effect of CO_2 forcing experiences large uncertainty. Nevertheless, the CO_2 variation itself cannot interpret the strengthening of wind along the Somali jet or the evolution of SASM precipitation intensity as inferred from reconstructions.

The two sites, ODP 359 and 758, situated in the inner sea of the Maldives and the southern Bay of Bengal, respectively, indicate an abrupt strengthening of monsoonal circulations in the SASM regions at 12.9 and 13.9 Ma, respectively. However, our modeling efforts cannot replicate these enhancements through either the uplift of the IP and HM or a reduction in CO_2 levels. Hence, it is likely that other factors exert a more significant influence on the reorganization of the SASM system. Examples include Antarctic glaciation, as suggested in Ali et al. (2021) and Sarr et al. (2022), as well as the closure of the Tethys, as discussed in research by Betzler et al. (2016) and Bialik et al. (2020).

5.2 Comparison with previous modeling studies

Concerning the effect of uplifted HM and IP on the SASM, our modeling results confirm the intensified SASM linked with the uplift of the IP (Liu et al., 2017; Zhang et al., 2015; Acosta and Huber, 2020; Tardif et al., 2020, 2023) rather than the HM (Zhang et al., 2012), particularly over the western region, i.e., from the Arabian Sea to northwestern India and Pakistan. When the evolution history of the HM–TP is taken into account, the uplift of the HM against the TP mainly enhances the orographic precipitation along the windward side of the HM and has little impact on regional monsoonal precipitation. While the effects of IP uplift from our AOGCM simulations qualitatively agree with previous studies using AGCMs (Wu et al., 2012; Liu et al., 2017; Acosta and Huber, 2020; Zhang et al., 2015), additional analysis (not shown) reveals notable impacts on ocean circulations. These impacts are evidenced by changes in sea surface temperatures (SSTs) and precipitation in tropical oceans, potentially influencing the SASM intensity through teleconnection. However, further discussion on the added value of AOGCM extends beyond the scope of our current study.

Regarding the mechanism of the IP uplift on the SASM, our analyses tend to support its thermal forcing effect (Wu et al., 2012; Liu et al., 2017), but instead of emphasizing the sensible heating effect, we highlight latent heating as a crucial link between the convection activity and regional circulations, as in a previous study (He, 2017). This demonstrates that it is not only temperature but also hydrological cycle modifications, as depicted in Sect. 4, that must be taken into account to understand the physical process involved. We also note that the IP's blocking/mechanical effect is much weaker in our study than that reported in Tang et al. (2013). In their study, the elevated IP effectively blocked the westerly flow to the south of the HM, facilitating the moisture advection from the Bay of Bengal into northern India and thus strongly enhancing the SASM precipitation, particularly in eastern India. A similar blocking effect (or role of gatekeeper) is also reported by Acosta and Huber (2020). Both studies utilized high spatial resolution models and were conducted using modern geographies. The weak blocking effect in our study is likely due to the (1) smaller size of the IP in the Miocene than in the present day and the (2) spatial lower-resolution model than that used in their studies ($\sim 1^\circ$ or higher); thus, some critical regional circulations linked to the SASM are likely misrepresented (Boos and Hurley, 2013; Acosta and Huber, 2017).

5.3 Uncertainty and methodological limitation

Geography, particularly the land–sea distribution, is another important driver for Asian monsoon development (Ramstein et al., 1997; Farnsworth et al., 2019; Sarr et al., 2022; Tardif et al., 2023). The land–sea distribution used in our Miocene simulations, like other reconstructions (Herold et al., 2008; He et al., 2021), inevitably contains uncertainties. For instance, the Bohai Bay and Yellow Sea basins in east Asia are open in the F18, contrary to the regional stratigraphy and lithofacial records (Tan et al., 2020). The Greenland–Scotland Ridge in F18 is set as ~ 4000 m, which is significantly deeper than the middle bathyal environment ($<$ 1000 m deep) indicated by geological evidence (Stoker et al., 2005). Large uncertainties are also present in the Tethys–Paratethys configuration. The Tethyan seaway is open, with a depth of over 3000 m in F18, in contrast to geological evidence suggesting intermittent openings during $\sim$ 15–12.8 Ma (Sun et al., 2021). The Paratethys was intermittently connected and disconnected from the global ocean during the Middle Miocene, according to geological studies (Rögl, 1998). It is assigned to connect to the global ocean in F18 and

Herold et al. (2008), while it retreats to the Carpathian–Black Sea–Caspian Sea region and is connected with the Mediterranean in He et al. (2021). In short, the Tethys–Paratethys configuration in F18 reflects more the features of early Middle Miocene geography with an open Tethyan seaway and a smaller IP. However, given that most reconstruction records focus on the late Middle Miocene period (14–12 Ma), our Middle Miocene simulations may not adequately capture the IP's effects and may be less suitable for comparison with proxy data. Nonetheless, a previous study (Sarr et al., 2022) utilizing a Late Miocene (10 Ma) configuration also emphasized the significant role of the Anatolia–Iran uplift on the enhanced SASM. Their experiments showed that this uplift deepened the low-pressure area over the Arabian Peninsula, intensifying low-level wind and moisture transport from the Arabian Sea towards South Asia, which is a process consistent with our simulations (Fig. 4a). We thus emphasize that constraining the exact timing of IP uplift is crucial to improve our understanding of the evolution of the SAM. During the late Middle Miocene period, significant geological events occurred, including the final closure of the Tethyan seaway $\sim$ 14 Ma (Sun et al., 2021) and the remarkable expansion of the Antarctic ice sheets from $\sim$ 14.2 to 13.8 Ma (Holbourn et al., 2005), resulting in global sea level changes. These geological events likely led to considerable changes in the physiography of the Middle East and eastern Africa. Consequently, the atmospheric and oceanic circulations in these regions and beyond are likely altered during the late Middle Miocene (Hamon et al., 2013). But some modeling studies indicated that "the sole effect of the Tethys way closure, without strong modification of land extension in the Arabian Peninsula region, remain limited" (Tardif et al., 2023), thereby not supporting the hypothesis that the closure of the Tethys seaway may contribute to altering the intensity of the monsoon during the Miocene (Bialik et al., 2020; Sun et al., 2021).

The uncertainty regarding the effects of CO_2 on SASM primarily arises from the wide range of estimated CO_2 values during the Middle Miocene. While our CO_2 sensitivity experiments cover various concentrations, prior studies (Thomson et al., 2021) indicate that the impacts of CO_2 variation on SASM are influenced by the background state. For instance, the status of the Tethys Sea, whether open or closed, introduces uncertain changes in the SASM rainfall. Consequently, understanding the precise impacts of the CO_2 variation on the SASM behavior remains complex and warrants further investigation. In brief, the evolution of the SASM during the Middle Miocene could have been caused by a combination of changes in topography in the east African and Middle Eastern physiography, CO_2 variation, and the progressive cryosphere expansion in Antarctica. All of these factors should be addressed in a future study with a careful experimental design.

A high-resolution model is essential for capturing the monsoon dynamics and thermodynamics to thus improve our understanding of the monsoonal variation/change (Acosta and Huber, 2017; Anand et al., 2018; Botsyun et al., 2022a, b). The climate model employed in the present study is a version of the low spatial resolution and not sufficient to reproduce the regional features of the SASM. For instance, the Indo-Gangetic low-level jet, a key mechanism that introduces the monsoon onshore flow from the Bay of Bengal into northern India (Acosta and Huber, 2017), is missing from our modern simulation (just as all the low-resolution models are). Misrepresentation of this circulation is problematic when interpreting the effect of HM uplift and reconciling the modeling–proxy data discrepancy (Toohey et al., 2014; Vogeli et al., 2018; Bhatia et al., 2021). The low resolution also likely underestimates the barrier effect of the IP due to topography smoothing (Boos and Hurley, 2013). For instance, the mechanical blocking effect is more prominent in the studies with high-resolution models (Tang et al., 2013; Acosta and Huber, 2020) than those with coarse-resolution models (Zhang et al., 2015; Wu et al., 2007). Although we are using computer resources to run coupled paleoclimate simulations and perform many sensitivity experiments with a high-resolution version, we acknowledge that a better understanding of the impact of the topographic change on the SASM and the underlying mechanism would benefit from additional simulations performed with an increased spatial resolution.

The evolution of the SASM is also largely determined by the large-scale circulation (Wu et al., 2012; Botsyun et al., 2022a). For instance, the mid-latitude westerly jet migrated earlier (in the year) and reached a higher latitude during the warm climate periods than in the pre-industrial period (Botsyun et al., 2022b). Our Miocene experiments likely confirm this point (not shown), but an in-depth investigation needs to be done in the future. We also acknowledge that running AOGCMs necessitates an extended period to achieve equilibrium. Particularly with significant modifications to topography or CO_2 levels, integrations spanning 200/500 years may carry the risk of non-equilibrium, potentially affecting the quantitative estimation of their effects but not essentially changing the results.

6 Conclusions

In this study, we performed a series of 12 experiments with the fully coupled AOGCM CESM1.2 (with $\sim 2^\circ$ horizontal resolution) to investigate the SASM in response to topographic changes in the region surrounding the Tibetan Plateau and the variations in the global CO_2 concentration during the Middle Miocene. We examined the effect of the elevated IP and HM on the SASM through a set of topographic sensitivity experiments. Additionally, due to the large uncertainties in the CO_2 reconstructions (Rae et al., 2021; CenCO_2pip, 2023), we conducted a series of CO_2 sensitivity experiments to investigate its impact on the SASM. We explored the underlying mechanisms and compared the

modeling results with proxy data. The conclusions are as follows:

1. We confirm and extend previous studies showing that IP uplift plays a major role in the intensification of the SASM, particularly in the western region, from the northern Arabian Sea to northwestern India and Pakistan, while it has little impact on eastern India. The effect of the HM uplift is confined to the range of the HM and its vicinity, producing an orographic precipitation change.

2. The response of the SASM to CO_2 variation under Middle Miocene boundary conditions is similar to that under present-day conditions projecting future SASM changes. This suggests that similar physical processes operate during these two warm periods. Enhanced monsoonal precipitation is primarily governed by enhanced thermodynamic conditions due to atmospheric warming, while the contribution from the change in large-scale monsoon circulation plays a secondary role. In the western region, topographic change, particularly the IP uplift, remains the dominant factor.

3. Topographic changes out-compete CO_2 variations in driving the intensification of the SASM. The forcing of the CO_2 variation is more important for the change in large-scale monsoon circulation that is decoupled with the rainfall change. In the case of strong CO_2 variation, that is, from 280 to 1000 ppm, similar to the abrupt $3\times$ or $4\times$ CO_2 experiments, its contribution to SASM precipitation is comparable (approximately 75 %–100 %) to that of topographic forcing in the core SAM region. However, in the western region, topographic forcing remains the dominant factor.

4. We propose a thermodynamic process linking the uplift of the IP to enhanced SASM, where a deepened thermal low transports moisture from the Arabian Sea to the western region, coupled with the South Asian High linked by latent heat release. However, the strong thermal effect of the uplifted IP in our Middle Miocene simulation is possibly associated with the smaller size of the IP and model's low resolution, which tends to underestimate the mechanical effects.

5. Compared with reconstructions, the effect of IP uplift is in good agreement with the observed evolution of precipitation and the change in the wind intensity, while the effects of the HM uplift and CO_2 variation are insufficient to interpret the proxies.

Code availability. The data in this study were analyzed and the figures were created with the NCAR Command Language. All relevant codes used in this work are available, upon request, from the corresponding author, Yan Zhao.

Data availability. The processed model outputs used to reproduce the figures in this work are archived in a Zenodo repository at https://doi.org/10.5281/zenodo.12201243 (Zuo et al., 2024). Instructions and permissions for the relevant experiments will be provided upon request to the corresponding author. The source code of CESM1.2 can be downloaded from https://www2.cesm.ucar.edu/models/cesm1.2/ (CESM Home, 2020).

Supplement. The supplement related to this article is available online at: https://doi.org/10.5194/cp-20-1817-2024-supplement.

Author contributions. MZ and YZ wrote the draft and analyzed the simulations. YS performed the simulations. GR and TZ modified the draft and particularly corrected the abstract and conclusions. YZ and DL conceived and developed the research. All authors participated in the final version of the paper.

Competing interests. The contact author has declared that none of the authors has any competing interests.

Disclaimer. Publisher's note: Copernicus Publications remains neutral with regard to jurisdictional claims made in the text, published maps, institutional affiliations, or any other geographical representation in this paper. While Copernicus Publications makes every effort to include appropriate place names, the final responsibility lies with the authors. Regarding the maps used in this paper, please note that Figs. 1–5 and 9 contain disputed territories.

Acknowledgements. This work has been jointly supported by the National Natural Science Foundation of China (grant nos. 41988101 and 42105047) and by the Second Tibetan Plateau Scientific Expedition and Research Program (STEP; grant no. 2019QZKK0708). Model simulations presented in this study were performed on the supercomputer of the Chinese Academy of Sciences, Jin Cloud.

Financial support. This research has been supported by the National Natural Science Foundation of China (grant nos. 41988101 and 42105047) and the Second Tibetan Plateau Scientific Expedition and Research Program (STEP; grant nos. 2019QZKK0708).

Review statement. This paper was edited by Zhongshi Zhang and reviewed by three anonymous referees.

References

Acosta, R. P. and Huber, M.: The neglected Indo-Gangetic Plains low-level jet and its importance for moisture transport and precipitation during the peak summer monsoon, Geophys. Res. Lett., 44, 8601–8610, https://doi.org/10.1002/2017gl074440, 2017.

Acosta, R. P. and Huber, M.: Competing Topographic Mechanisms for the Summer Indo-Asian Monsoon, Geophys. Res. Lett., 47, e2019GL085112, https://doi.org/10.1029/2019gl085112, 2020.

Agard, P., Omrani, J., Jolivet, L., Whitechurch, H., Vrielynck, B., Spakman, W., MoniÉ, P., Meyer, B., and Wortel, R.: Zagros orogeny: a subduction-dominated process, Geolog. Mag., 148, 692–725, https://doi.org/10.1017/S001675681100046X, 2011.

Ali, S., Hathorne, E. C., and Frank, M.: Persistent Provenance of South Asian Monsoon-Induced Silicate Weathering Over the Past 27 Million Years, Paleoceanogr. Paleoclimatol., 36, e2020PA003909, https://doi.org/10.1029/2020pa003909, 2021.

An, Z. S., Kutzbach, J. E., Prell, W. L., and Porter, S. C.: Evolution of Asian monsoons and phased uplift of the Himalayan Tibetan plateau since Late Miocene times, Nature, 411, 62–66, 2001.

Anand, A., Mishra, S. K., Sahany, S., Bhowmick, M., Rawat, J. S., and Dash, S. K.: Indian Summer Monsoon Simulations: Usefulness of Increasing Horizontal Resolution, Manual Tuning, and Semi-Automatic Tuning in Reducing Present-Day Model Biases, Sci. Rep., 8, 3522, https://doi.org/10.1038/s41598-018-21865-1, 2018.

Ballato, P., Cifelli, F., Heidarzadeh, G., Ghassemi, M. R., Wickert, A. D., Hassanzadeh, J., Dupont-Nivet, G., Balling, P., Sudo, M., Zeilinger, G., Schmitt, A. K., Mattei, M., and Strecker, M. R.: Tectono-sedimentary evolution of the northern Iranian Plateau: insights from middle–late Miocene foreland-basin deposits, Basin Res., 29, 417–446, https://doi.org/10.1111/bre.12180, 2017.

Betzler, C., Eberli, G. P., Kroon, D., Wright, J. D., Swart, P. K., Nath, B. N., Alvarez-Zarikian, C. A., Alonso-Garcia, M., Bialik, O. M., Blattler, C. L., Guo, J. A., Haffen, S., Horozal, S., Inoue, M., Jovane, L., Lanci, L., Laya, J. C., Mee, A. L. H., Luedmann, T., Nakakuni, M., Niino, K., Petruny, L. M., Pratiwi, S. D., Reijmer, J. J. G., Reolid, J., Slagle, A. L., Sloss, C. R., Su, X., Yao, Z., and Young, J. R.: The abrupt onset of the modern South Asian Monsoon winds, Sci. Rep., 6, 29838, https://doi.org/10.1038/srep29838, 2016.

Bhatia, H., Srivastava, G., Spicer, R. A., Farnsworth, A., Spicer, T. E. V., Mehrotra, R. C., Paudayal, K. N., and Valdes, P.: Leaf physiognomy records the Miocene intensification of the South Asia Monsoon, Global Planet. Change, 196, 103365, https://doi.org/10.1016/j.gloplacha.2020.103365, 2021.

Bialik, O. M., Auer, G., Ogawa, N. O., Kroon, D., Waldmann, N. D., and Ohkouchi, N.: Monsoons, Upwelling, and the Deoxygenation of the Northwestern Indian Ocean in Response to Middle to Late Miocene Global Climatic Shifts, Paleoceanogr. Paleoclimatol., 35, e2019PA003762, https://doi.org/10.1029/2019pa003762, 2020.

Boos, W. R. and Hurley, J. V.: Thermodynamic Bias in the Multimodel Mean Boreal Summer Monsoon, J. Climate, 26, 2279–2287, https://doi.org/10.1175/jcli-d-12-00493.1, 2013.

Boos, W. R. and Kuang, Z.: Dominant control of the South Asian monsoon by orographic insulation versus plateau heating, Nature, 463, 218–222, https://doi.org/10.1038/nature08707, 2010.

Botsyun, S., Mutz, S. G., Ehlers, T. A., Koptev, A., Wang, X., Schmidt, B., Appel, E., and Scherer, D. E.: Influence of Large-Scale Atmospheric Dynamics on Precipitation Seasonality of the Tibetan Plateau and Central Asia in Cold and Warm Climates During the Late Cenozoic, J. Geophys. Res.-Atmos., 127, e2021JD035810, https://doi.org/10.1029/2021jd035810, 2022a.

Botsyun, S., Ehlers, T. A., Koptev, A., Böhme, M., Methner, K., Risi, C., Stepanek, C., Mutz, S. G., Werner, M., Boateng, D., and Mulch, A.: Middle Miocene Climate and Stable Oxygen Isotopes in Europe Based on Numerical Modeling, Paleoceanogr. Paleoclimatol., 37, e2022PA004442, https://doi.org/10.1029/2022PA004442, 2022b.

Burls, N. J., Bradshaw, C. D., De Boer, A. M., Herold, N., Huber, M., Pound, M., Donnadieu, Y., Farnsworth, A., Frigola, A., Gasson, E., von der Heydt, A. S., Hutchinson, D. K., Knorr, G., Lawrence, K. T., Lear, C. H., Li, X., Lohmann, G., Lunt, D. J., Marzocchi, A., Prange, M., Riihimaki, C. A., Sarr, A. C., Siler, N., and Zhang, Z.: Simulating Miocene Warmth: Insights From an Opportunistic Multi-Model Ensemble (MioMIP1), Paleoceanogr. Paleoclimatol., 36, e2020PA004054, https://doi.org/10.1029/2020pa004054, 2021.

CenCO$_2$PIP: Toward a Cenozoic history of atmospheric CO$_2$, Science, 382, eadi5177, https://doi.org/10.1126/science.adi5177, 2023.

CESM Home: CESM Models, https://www2.cesm.ucar.edu/models/cesm1.2/ (last access: 4 August 2024), 2020.

Chakraborty, A., Nanjundiah, R. S., and Srinivasan, J.: Theoretical aspects of the onset of Indian summer monsoon from perturbed orography simulations in a GCM, Ann. Geophys., 24, 2075–2089, https://doi.org/10.5194/angeo-24-2075-2006, 2006.

Chen, G. S., Liu, Z., and Kutzbach, J. E.: Reexamining the barrier effect of the Tibetan Plateau on the South Asian summer monsoon, Clim. Past, 10, 1269–1275, https://doi.org/10.5194/cp-10-1269-2014, 2014.

Chou, C., Neelin, J. D., Chen, C.-A., and Tu, J.-Y.: Evaluating the "Rich-Get-Richer" Mechanism in Tropical Precipitation Change under Global Warming, J. Climate, 22, 1982–2005, https://doi.org/10.1175/2008jcli2471.1, 2009.

Clift, P. D. and Webb, A. A. G.: A history of the Asian monsoon and its interactions with solid Earth tectonics in Cenozoic South Asia, Geol. Soc. Lond. Spec. Publ., 483, 631–652, https://doi.org/10.1144/SP483.1, 2019.

Clift, P. D., Hodges, K. V., Heslop, D., Hannigan, R., Van Long, H., and Calves, G.: Correlation of Himalayan exhumation rates and Asian monsoon intensity, Nat. Geosci., 1, 875–880, https://doi.org/10.1038/ngeo351, 2008.

Ding, L., Spicer, R. A., Yang, J., Xu, Q., Cai, F., Li, S., Lai, Q., Wang, H., Spicer, T. E. V., Yue, Y., Shukla, A., Srivastava, G., Khan, M. A., Bera, S., and Mehrotra, R.: Quantifying the rise of the Himalaya orogen and implications for the South Asian monsoon, Geology, 45, 215–218, https://doi.org/10.1130/g38583.1, 2017.

Ding, L., Kapp, P., Cai, F., Garzione, C. N., Xiong, Z., Wang, H., and Wang, C.: Timing and mechanisms of Tibetan Plateau uplift, Nat. Rev. Earth Environ., 3, 652–667, https://doi.org/10.1038/s43017-022-00318-4, 2022.

Endo, H. and Kitoh, A.: Thermodynamic and dynamic effects on regional monsoon rainfall changes in a warmer climate, Geophys. Res. Lett., 41, 1704–1710, https://doi.org/10.1002/2013gl059158, 2014.

Eyring, V., Bony, S., Meehl, G. A., Senior, C. A., Stevens, B., Stouffer, R. J., and Taylor, K. E.: Overview of the Coupled Model Intercomparison Project Phase 6 (CMIP6) experimental design and organization, Geosci. Model Dev., 9, 1937–1958, https://doi.org/10.5194/gmd-9-1937-2016, 2016.

Farnsworth, A., Lunt, D. J., Robinson, S. A., Valdes, P. J., Roberts, W. H. G., Clift, P. D., Markwick, P., Su, T., Wrobel, N., Bragg, F., Kelland, S.-J., and Pancost, R. D.: Past East Asian monsoon evolution controlled by paleogeography, not CO_2, Sci. Adv., 5, eaax1697, https://doi.org/10.1126/sciadv.aax1697, 2019.

Fluteau, F., Ramstein, G., and Besse, J.: Simulating the evolution of the Asian and African monsoons during the past 30 Myr using an atmospheric general circulation model, J. Geophys. Res.-Atmos., 104, 11995–12018, https://doi.org/10.1029/1999JD900048, 1999.

Foster, G. L. and Rohling, E. J.: Relationship between sea level and climate forcing by CO_2 on geological timescales, P. Natl. Acad. Sci. USA, 110, 1209–1214, https://doi.org/10.1073/pnas.1216073110, 2013.

Frigola, A., Prange, M., and Schulz, M.: Boundary conditions for the Middle Miocene Climate Transition (MMCT v1.0), Geosci. Model Dev., 11, 1607–1626, https://doi.org/10.5194/gmd-11-1607-2018, 2018.

Gent, P. R., Danabasoglu, G., Donner, L. J., Holland, M. M., Hunke, E. C., Jayne, S. R., Lawrence, D. M., Neale, R. B., Rasch, P. J., Vertenstein, M., Worley, P. H., Yang, Z.-L., and Zhang, M.: The Community Climate System Model Version 4, J. Climate, 24, 4973–4991, https://doi.org/10.1175/2011jcli4083.1, 2011.

Goldner, A., Herold, N., and Huber, M.: The challenge of simulating the warmth of the mid-Miocene climatic optimum in CESM1, Clim. Past, 10, 523–536, https://doi.org/10.5194/cp-10-523-2014, 2014.

Gupta, A. K., Yuvaraja, A., Prakasam, M., Clemens, S. C., and Velu, A.: Evolution of the South Asian monsoon wind system since the late Middle Miocene, Palaeogeogr. Palaeocl. Palaeoecol., 438, 160–167, https://doi.org/10.1016/j.palaeo.2015.08.006, 2015.

Hamon, N., Sepulchre, P., Lefebvre, V., and Ramstein, G.: The role of eastern Tethys seaway closure in the Middle Miocene Climatic Transition (ca. 14 Ma), Clim. Past, 9, 2687–2702, https://doi.org/10.5194/cp-9-2687-2013, 2013.

Harris, N.: The elevation history of the Tibetan Plateau and its implications for the Asian monsoon, Palaeogeogr. Palaeocl. Palaeoecol., 241, 4–15, https://doi.org/10.1016/j.palaeo.2006.07.009, 2006.

He, B.: Influences of elevated heating effect by the Himalaya on the changes in Asian summer monsoon, Theor. Appl. Climatol., 128, 905–917, https://doi.org/10.1007/s00704-016-1746-5, 2017.

He, Z., Zhang, Z., Guo, Z., Scotese, C. R., and Deng, C.: Middle Miocene ($\sim$ 14 Ma) and Late Miocene ($\sim$ 6 Ma) Paleogeographic Boundary Conditions, Paleoceanogr. Paleoclimatol., 36, e2021PA004298, https://doi.org/10.1029/2021pa004298, 2021.

Herold, N., Seton, M., Mueller, R. D., You, Y., and Huber, M.: Middle Miocene tectonic boundary conditions for use in climate models, Geochem. Geophy. Geosy., 9, Q10009, https://doi.org/10.1029/2008gc002046, 2008.

Herold, N., Huber, M., and Mueller, R. D.: Modeling the Miocene Climatic Optimum. Part I: Land and Atmosphere, J. Climate, 24, 6353–6372, https://doi.org/10.1175/2011jcli4035.1, 2011.

Hersbach, H., Bell, B., Berrisford, P., Hirahara, S., Horanyi, A., Munoz-Sabater, J., Nicolas, J., Peubey, C., Radu, R., Schepers, D., Simmons, A., Soci, C., Abdalla, S., Abellan, X., Balsamo, G., Bechtold, P., Biavati, G., Bidlot, J., Bonavita, M., De Chiara, G., Dahlgren, P., Dee, D., Diamantakis, M., Dragani, R., Flemming, J., Forbes, R., Fuentes, M., Geer, A., Haimberger, L., Healy, S., Hogan, R. J., Holm, E., Janiskova, M., Keeley, S., Laloyaux, P., Lopez, P., Lupu, C., Radnoti, G., de Rosnay, P., Rozum, I., Vamborg, F., Villaume, S., and Thepaut, J. N.: The ERA5 global reanalysis, Q. J. Roy. Meteorol. Soc., 146, 1999–2049, https://doi.org/10.1002/qj.3803, 2020.

Holbourn, A., Kuhnt, W., Schulz, M., and Erlenkeuser, H.: Impacts of orbital forcing and atmospheric carbon dioxide on Miocene ice-sheet expansion, Nature, 438, 483–487, https://doi.org/10.1038/nature04123, 2005.

Huffman, G. J., Adler, R. F., Bolvin, D. T., and Gu, G.: Improving the global precipitation record: GPCP Version 2.1, Geophys. Res. Lett., 36, L17808, https://doi.org/10.1029/2009gl040000, 2009.

Hunke, E. C. and Lipscomb, W. H.: CICE: the Los Alamos Sea Ice Model Documentation and Software User's Manual Version 4, https://csdms.colorado.edu/w/images/CICE_documentation_and_software_user's_manual.pdf (last access: 4 August 2024), 1–76, 2010.

Jin, C., Wang, B., and Liu, J.: Future Changes and Controlling Factors of the Eight Regional Monsoons Projected by CMIP6 Models, J. Climate, 33, 9307–9326, https://doi.org/10.1175/jcli-d-20-0236.1, 2020.

Kitoh, A.: Effects of Large-Scale Mountains on Surface Climate – A Coupled Ocean-Atmosphere General Circulation Model Study, J. Meteorol. Soc. Jpn. Ser. II, 80, 1165–1181, https://doi.org/10.2151/jmsj.80.1165, 2002.

Kong, Y., Wu, Y., Hu, X., Li, Y., and Yang, S.: Uncertainty in projections of the South Asian summer monsoon under global warming by CMIP6 models: Role of tropospheric meridional thermal contrast, Atmos. Ocean. Sci. Lett., 15, 100145, https://doi.org/10.1016/j.aosl.2021.100145, 2022.

Krapp, M. and Jungclaus, J. H.: The Middle Miocene climate as modelled in an atmosphere-ocean-biosphere model, Clim. Past, 7, 1169–1188, https://doi.org/10.5194/cp-7-1169-2011, 2011.

Kutzbach, J. E., Guetter, P. J., Ruddiman, W. F., and Prell, W. L.: Sensitivity of climate to late Cenozoic uplift in southern Asia and the American west: Numerical experiments, J. Geophys. Res.-Atmos., 94, 18393–18407, https://doi.org/10.1029/JD094iD15p18393, 1989.

Lawrence, D. M., Oleson, K. W., Flanner, M. G., Thornton, P. E., Swenson, S. C., Lawrence, P. J., Zeng, X., Yang, Z.-L., Levis, S., Sakaguchi, K., Bonan, G. B., and Slater, A. G.: Parameterization improvements and functional and structural advances in Version 4 of the Community Land Model, J. Adv. Model. Earth Syst., 3, M03001, https://doi.org/10.1029/2011MS00045, 2011.

Licht, A., van Cappelle, M., Abels, H. A., Ladant, J. B., Trabucho-Alexandre, J., France-Lanord, C., Donnadieu, Y., Vandenberghe, J., Rigaudier, T., Lécuyer, C., Terry Jr., D., Adriaens, R., Boura, A., Guo, Z., Soe, A. N., Quade, J., Dupont-Nivet, G., and Jaeger, J. J.: Asian monsoons in a late Eocene greenhouse world, Nature, 513, 501–506, https://doi.org/10.1038/nature13704, 2014.

Liu, X., Xu, Q., and Ding, L.: Differential surface uplift: Cenozoic paleoelevation history of the Tibetan Plateau, Sci. China Earth Sci., 59, 2105–2120, https://doi.org/10.1007/s11430-015-5486-y, 2016.

Liu, Y., Wang, Z., Zhuo, H., and Wu, G.: Two types of summertime heating over Asian large-scale orography and excitation of potential-vorticity forcing II. Sensible heating over Tibetan-Iranian Plateau, Sci. China Earth Sci., 60, 733–744, https://doi.org/10.1007/s11430-016-9016-3, 2017.

Macgregor, D.: History of the development of the East African Rift System: A series of interpreted maps through time, J. Afr. Earth Sci., 101, 232–252, https://doi.org/10.1016/j.jafrearsci.2014.09.016, 2015.

Manabe, S. and Terpstra, T. B.: The Effects of Mountains on the General Circulation of the Atmosphere as Identified by Numerical Experiments, J. Atmos. Sci., 31, 3–42, https://doi.org/10.1175/1520-0469(1974)031<0003:TEOMOT>2.0.CO;2, 1974.

McQuarrie, N., Stock, J. M., Verdel, C., and Wernicke, B. P.: Cenozoic evolution of Neotethys and implications for the causes of plate motions, Geophys. Res. Lett., 30, 2036, https://doi.org/10.1029/2003GL017992, 2003.

Medina, S., Houze Jr., R. A., Kumar, A., and Niyogi, D.: Summer monsoon convection in the Himalayan region: terrain and land cover effects, Q. J. Roy. Meteorol. Soc., 136, 593–616, https://doi.org/10.1002/qj.601, 2010.

Miao, Y., Fang, X., Sun, J., Xiao, W., Yang, Y., Wang, X., Farnsworth, A., Huang, K., Ren, Y., Wu, F., Qiao, Q., Zhang, W., Meng, Q., Yan, X., Zheng, Z., Song, C., and Utescher, T.: A new biologic paleoaltimetry indicating Late Miocene rapid uplift of northern Tibet Plateau, Science, 378, 1074–1079, https://doi.org/10.1126/science.abo2475, 2022.

Mouthereau, F.: Timing of uplift in the Zagros belt/Iranian plateau and accommodation of late Cenozoic Arabia–Eurasia convergence, Geolog. Mag., 148, 726–738, https://doi.org/10.1017/S0016756811000306, 2011.

Neale, R. B., Richter, J., Park, S., Lauritzen, P. H., Vavrus, S. J., Rasch, P. J., and Zhang, M.: The Mean Climate of the Community Atmosphere Model (CAM4) in Forced SST and Fully Coupled Experiments, J. Climate, 26, 5150–5168, https://doi.org/10.1175/JCLI-D-12-00236.1, 2013.

Pagani, M., Arthur, M. A., and Freeman, K. H.: Miocene evolution of atmospheric carbon dioxide, Paleoceanography, 14, 273–292, https://doi.org/10.1029/1999pa900006, 1999.

Prell, W. L. and Kutzbach, J. E.: Sensitivity Of The Indian Monsoon To Forcing Parameters And Implications For Its Evolution, Nature, 360, 647–652, https://doi.org/10.1038/360647a0, 1992.

Rae, J. W. B., Zhang, Y. G., Liu, X., Foster, G. L., Stoll, H. M., and Whiteford, R. D. M.: Atmospheric CO_2 over the Past 66 Million Years from Marine Archives, Annu. Rev. Earth Planet. Sci., 49, 609–641, https://doi.org/10.1146/annurev-earth-082420-063026, 2021.

Ramstein, G., Fluteau, F., Besse, J., and Joussaume, S.: Effect of orogeny, plate motion and land–sea distribution on Eurasian climate change over the past 30 million years, Nature, 386, 788–795, https://doi.org/10.1038/386788a0, 1997.

Reuter, M., Piller, W. E., Harzhauser, M., and Kroh, A.: Cyclone trends constrain monsoon variability during late Oligocene sea level highstands (Kachchh Basin, NW India), Clim. Past, 9, 2101–2115, https://doi.org/10.5194/cp-9-2101-2013, 2013.

Rögl, F.: Palaeogeographic Considerations for Mediterranean and Paratethys Seaways (Oligocene to Miocene), Ann. Naturhist. Mus. Wien, 99A, 279–310, 1998.

Sarr, A.-C., Donnadieu, Y., Bolton, C. T., Ladant, J.-B., Licht, A., Fluteau, F., Laugie, M., Tardif, D., and Dupont-Nivet, G.: Neogene South Asian monsoon rainfall and wind histories diverged due to topographic effects, Nat. Geosci., 15, 314–319, https://doi.org/10.1038/s41561-022-00919-0, 2022.

Smith, R., Jones, P., Briegleb, B., Bryan, F., and Yeager, S.: The parallel ocean program (pop) reference manual: Ocean component of the community climate system model (ccsm), https://www2.cesm.ucar.edu/models/cesm1.0/pop2/doc/sci/POPRefManual.pdf (last access: 4 August 2024), 2010.

Spicer, R. A.: Tibet, the Himalaya, Asian monsoons and biodiversity – In what ways are they related?, Plant Divers., 39, 233–244, https://doi.org/10.1016/j.pld.2017.09.001, 2017.

Srivastava, G., Paudayal, K. N., Utescher, T., and Mehrotra, R. C.: Miocene vegetation shift and climate change: Evidence from the Siwalik of Nepal, Global Planet. Change, 161, 108–120, https://doi.org/10.1016/j.gloplacha.2017.12.001, 2018.

Steinthorsdottir, M., Coxall, H. K., de Boer, A. M., Huber, M., Barbolini, N., Bradshaw, C. D., Burls, N. J., Feakins, S. J., Gasson, E., Henderiks, J., Holbourn, A. E., Kiel, S., Kohn, M. J., Knorr, G., Kurschner, W. M., Lear, C. H., Liebrand, D., Lunt, D. J., Mors, T., Pearson, P. N., Pound, M. J., Stoll, H., and Stromberg, C. A. E.: The Miocene: The Future of the Past, Paleoceanogr. Paleoclimatol., 36, e2020PA004037, https://doi.org/10.1029/2020pa004037, 2021.

Stoker, M. S., Praeg, D., Hjelstuen, B. O., Laberg, J. S., Nielsen, T., and Shannon, P. M.: Neogene stratigraphy and the sedimentary and oceanographic development of the NW European Atlantic margin, Mar. Petrol. Geol., 22, 977–1005, 2005.

Su, B., Jiang, D., Zhang, R., Sepulchre, P., and Ramstein, G.: Difference between the North Atlantic and Pacific meridional overturning circulation in response to the uplift of the Tibetan Plateau, Clim. Past, 14, 751–762, https://doi.org/10.5194/cp-14-751-2018, 2018.

Sun, J., Sheykh, M., Ahmadi, N., Cao, M., Zhang, Z., Tian, S., Sha, J., Jian, Z., Windley, B. F., and Talebian, M.: Permanent closure of the Tethyan Seaway in the northwestern Iranian Plateau driven by cyclic sea-level fluctuations in the late Middle Miocene, Palaeogeogr. Palaeocl. Palaeoecol., 564, 110172, https://doi.org/10.1016/j.palaeo.2020.110172, 2021.

Sun, Y., Wu, H., Ramstein, G., Liu, B., Zhao, Y., Li, L., Yuan, X., Zhang, W., Li, L., Zou, L., and Zhou, T.: Revisiting the physical mechanisms of East Asian summer monsoon precipitation changes during the mid-Holocene: a data–model comparison, Clim. Dynam., 60, 1009–1022, https://doi.org/10.1007/s00382-022-06359-1, 2023.

Tada, R., Zheng, H., and Clift, P. D.: Evolution and variability of the Asian monsoon and its potential linkage with uplift of the Himalaya and Tibetan Plateau, Progr. Earth Planet. Sci., 3, 4, https://doi.org/10.1186/s40645-016-0080-y, 2016.

Tan, M., Zhu, X., Liu, Q., Zhang, Z., and Liu, W.: Multiple fluvial styles in Late Miocene post-rift successions of the offshore Bohai Bay Basin (China): Evidence from a seismic geomorphological study, Mar. Petrol. Geol., 113, 104173, https://doi.org/10.1016/j.marpetgeo.2019.104173, 2020.

Tang, H., Micheels, A., Eronen, J. T., Ahrens, B., and Fortelius, M.: Asynchronous responses of East Asian and Indian summer monsoons to mountain uplift shown by regional climate modelling experiments, Clim. Dynam., 40, 1531–1549, https://doi.org/10.1007/s00382-012-1603-x, 2013.

Tardif, D., Fluteau, F., Donnadieu, Y., Le Hir, G., Ladant, J.-B., Sepulchre, P., Licht, A., Poblete, F., and Dupont-Nivet, G.: The

origin of Asian monsoons: a modelling perspective, Clim. Past, 16, 847–865, https://doi.org/10.5194/cp-16-847-2020, 2020.

Tardif, D., Sarr, A. C., Fluteau, F., Licht, A., Kaya, M., Ladant, J. B., Meijer, N., Donnadieu, Y., Dupont-Nivet, G., Bolton, C. T., Le Hir, G., Pillot, Q., Poblete, F., Sepulchre, P., Toumoulin, A., and Banfield, W.: The role of paleogeography in Asian monsoon evolution: a review and new insights from climate modelling, Earth-Sci. Rev., 243, 104464, https://doi.org/10.1016/j.earscirev.2023.104464, 2023.

Thomson, J. R., Holden, P. B., Anand, P., Edwards, N. R., Porchier, C. A., and Harris, N. B. W.: Tectonic and climatic drivers of Asian monsoon evolution, Nat. Commun., 12, 4022, https://doi.org/10.1038/s41467-021-24244-z, 2021.

Toohey, M., Krüger, K., Bittner, M., Timmreck, C., and Schmidt, H.: The impact of volcanic aerosol on the Northern Hemisphere stratospheric polar vortex: mechanisms and sensitivity to forcing structure, Atmos. Chem. Phys., 14, 13063–13079, https://doi.org/10.5194/acp-14-13063-2014, 2014.

Vogeli, N., Huyghe, P., van der Beek, P., Najman, Y., Garzanti, E., and Chauvel, C.: Weathering regimein the Eastern Himalaya since the mid-Miocene: indications fromdetrital geochemistry and claymineralogy of the Kameng River Section, Arunachal Pradesh, India, Basin Res., 30, 59–74, https://doi.org/10.1111/bre.12242, 2018.

Wang, B. and Ding, Q.: Global monsoon: Dominant mode of annual variation in the tropics, Dynam. Atmos. Oceans, 44, 165–183, https://doi.org/10.1016/j.dynatmoce.2007.05.002, 2008.

Wang, C., Dai, J., Zhao, X., Li, Y., Graham, S. A., He, D., Ran, B., and Meng, J.: Outward-growth of the Tibetan Plateau during the Cenozoic: A review, Tectonophysics, 621, 1–43, https://doi.org/10.1016/j.tecto.2014.01.036, 2014.

Webster, P. J. and Yang, S.: Monsoon and Enso: Selectively Interactive Systems, Q. J. Roy. Meteorol. Soc., 118, 877–926, https://doi.org/10.1002/qj.49711850705, 1992.

Wei, H.-H. and Bordoni, S.: On the Role of the African Topography in the South Asian Monsoon, J. Atmos. Sci., 73, 3197–3212, https://doi.org/10.1175/JAS-D-15-0182.1, 2016.

Wu, G., Liu, Y., Zhang, Q., Duan, A., Wang, T., Wan, R., Liu, X., Li, W., Wang, Z., and Liang, X.: The Influence of Mechanical and Thermal Forcing by the Tibetan Plateau on Asian Climate, J. Hydrometeorol., 8, 770–789, https://doi.org/10.1175/JHM609.1, 2007.

Wu, G., Liu, Y., He, B., Bao, Q., Duan, A., and Jin, F.-F.: Thermal Controls on the Asian Summer Monsoon, Sci. Rep., 2, 404, https://doi.org/10.1038/srep00404, 2012.

Yang, X., Groeneveld, J., Jian, Z., Steinke, S., and Giosan, L.: Middle Miocene Intensification of South Asian Monsoonal Rainfall, Paleoceanogr. Paleoclimatol., 35, e2020PA003853, https://doi.org/10.1029/2020pa003853, 2020.

Zhang, R., Jiang, D., Liu, X., and Tian, Z.: Modeling the climate effects of different subregional uplifts within the Himalaya-Tibetan Plateau on Asian summer monsoon evolution, Chinese Sci. Bull., 57, 4617–4626, https://doi.org/10.1007/s11434-012-5284-y, 2012.

Zhang, R., Jiang, D., Zhang, Z., and Yu, E.: The impact of regional uplift of the Tibetan Plateau on the Asian monsoon climate, Palaeogeogr. Palaeocl. Palaeoecol., 417, 137–150, https://doi.org/10.1016/j.palaeo.2014.10.030, 2015.

Zhang, R., Jiang, D., and Zhang, Z.: Vegetation and Ocean Feedbacks on the Asian Climate Response to the Uplift of the Tibetan Plateau, J. Geophys. Res.-Atmos., 124, 6327–6341, https://doi.org/10.1029/2019JD030503, 2019.

Zuo, M., Sun, Y., Zhao, Y., Ramstein, G., Ding, L., and Zhou, T.: Processed model outputs for "South Asian summer monsoon enhanced by the uplift of Iranian Plateau in Middle Miocene", Zenodo [data set], https://doi.org/10.5281/zenodo.12201243, 2024.